Towards Anion Photoelectron Spectroscopy – Optimisation of the Time-of-Flight Mass Spectrometer with Photoelectron Spectrometer in tandem

by

Henryk Quak

Under the supervision of

Dr. Duncan Wild

I certify that, the substance of this thesis has not previously been submitted for any degree or diploma and is not currently being submitted for any degree or diploma.

To the best of my knowledge, any help received in preparing this thesis, sources and references used, have been acknowledged.

_____

Henryk Quak Lin Hian

Abstract

A Time of Flight Mass Spectrometer coupled to a Photoelectron Spectrometer (TOF-PES) was modified for photoelectron spectroscopic studies on anionic gas phase clusters. The main principle for photoelectron investigation is essentially based on the measurement of the difference of the energy level during a neutral ← anion transition when the anionic cluster is excited by ultraviolet light.

The apparatus is still not fully operational and requires more optimisation before undertaking any experiments. Considering that the whole setup is comprised of two sensitive scientific apparatus in tandem, the optimisation process is tedious as the performance of the either apparatus will hamper the final outcome. Presented in this work are the details of the optimisations and modifications that were implemented, i.e. (i) calibration of the gas mixing station, (ii) optimisation of the time-of-flight mass spectrometry, (iii) modification of the safety system and (iv) laser alignment. The current capabilities of the TOF-PES will also be discussed with some of the mass spectra obtained for iodine and bromine complexes.

In preparation for intended photoelectron spectroscopy experiments, *ab initio* calculations were performed to predict the experimental spectra and a fluoride – acetylene complex was investigated. The optimised geometries of both the neutral and anion complexes of fluorine and acetylene were calculated along with their energetic values. Photoelectron spectra were predicted for this F·[HCCH] complex and a 5←0 transition was found to be the most probable.

Acknowledgements

I would like to acknowledge and thank my supervisor, Dr. Duncan Wild for his guidance and patience throughout the year, and introducing me to the world of electronics and computational chemistry.

To Dr. Allan McKinley: Thank you for the computer resources.

To the workshop staff: Nigel Hamilton, Andrew Sawyer, Damien Bainbridge and Trevor Franklin. I must thank you all for the wonderful support.

To Rob LaMacchia: Many thanks for showing me the ropes

And last of all to my family – it has been a long year.

Table of Contents

Table of Figures

1. Introduction and Theory

1.1 Introduction

Chemical reactions and processes are heavily involved in most of the activities that happen daily. A few important examples which are essential for maintaining biological life include proton transfer reactions, establishing electrochemical gradients and hydrogen bonding.[1, 2] Besides biology, chemical reactions involving ions and ionic complexes also occur in the atmosphere; one notorious example being the formation of acid rain. Despite the importance, little is known about the detailed nature of such processes and reactions. To unravel this paradox and achieve a better understanding of the chemistry, a logical approach is to investigate the intermolecular interactions between the reactive species. However before attempting any ambitious investigation such as probing intermolecular interactions in atmospheric chemistry, an essential precursor is a thorough understanding of the way in which an individual ion interacts with single molecule. This narrows the scope of investigation and defines an objective that can be realistically achieved.

Studies on ion–molecule interactions were made possible several decades ago when mass spectrometrists discovered that gas phase ions tended to form clusters with molecules present in surrounding gas. It is therefore possible to prepare charged complexes consisting of a single, or few, neutral molecules attached to an ion core.[3] The size of the clusters are governed by clustering equilibria,

$$A^{\pm} - L_n \;+\; L \;\leftrightarrow\; A^{\pm} - L_{n+1} \tag{1}$$
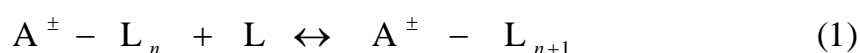
where $A^{\pm}$ is an atomic or molecular ion and L is a neutral atom or molecule which acts as a 'solvent'. One of the methods used in the initial studies of ion-molecule behaviour was high pressure mass spectrometry (HPMS). Equilibrium conditions

between the ions and molecules are attained in a high pressure cell and one then determines the cluster ion population by mass spectrometry.[4] The equilibrium constants measured over a range of temperature can be used to evaluate ion energetics using van't Hoff's relation, given by equation 2.

$$\ln K_{eq} = -\frac{\Delta H^{\circ}}{RT} + \frac{\Delta S^{\circ}}{R} \qquad (2)$$

Plotting $\ln K_{eq}$ against $\dfrac{1}{T}$ yields a "van't Hoff plot" and the solvent binding enthalpies (ΔH°) and entropies (ΔS°) can be readily determined. Information on kinetics can also be obtained from a similar experiment known as the pulsed, trapped ion cyclotron resonance (ICR) spectroscopy developed by McIver.[5] This involves trapping the product ions in the cell by a magnetic field in the z-axis, confining them to a circular orbit in the xy-plane by the static voltage plates, and subsequently detecting the amount of ions present from the power loss of an attached marginal oscillator. The angular frequency of the orbital motion is given by;

$$\omega_c = qB / mc \qquad (3)$$

where c is the speed of light, m and q are the mass and charge of the ions and B is the magnetic field strength. After a desired amount of interaction time, the presences of ions produced (with known *mass/charge*) are determined by pulsing the intensity of the magnetic field B from equation 3 to

$$\omega_c' = q(B + B') / mc \qquad (4)$$

such that ω_c' matches the RF frequency produced by the attached marginal oscillator. For example, at 153.57 kHz frequency produced by the marginal oscillator, nitrogen ions of mass 28 can only be detected when the magnetic field is 2800 G. Therefore, by pulsing $B' = 20$ G on top of the original magnetic field of $B = 2780$ G will matched

2

the resonance of the marginal oscillator and initiates the detection of nitrogen ions. Kinetics can be obtained by plotting the amount of ions detected against the duration of the B' pulse.

Physical data and information on the thermodynamics and kinetics of chemical reactions that has been well documented over the past fifty years are valuable but inadequate in providing a full understanding of intermolecular interactions, i.e. hydrogen bonding with halide. As such, the development of spectroscopic method in recent decades has been instrumental in augmenting these studies. Spectroscopy is a powerful tool and various groups[6-8] have employed different flavours of spectroscopy to probe the chemical and physical interaction of ion-molecules.

Studies on intermolecular interactions can also be carried out using theoretical approaches.[9] Theoretical studies on the electronic structure and molecular dynamics at the most basic level allow one to simulate ion-molecular interactions and predict the cluster geometrical structures. Data based on theoretical studies serve as guides to the interpretation of results gathered from an actual experiment. Hence, with the development of new models, it is natural that the collaboration between theories and experiments can allow one to even study interactions that cannot be easily observed with experiments.

This introduction will review the gas phase spectroscopy of ion-molecule complexes. However, given the wide range of spectroscopic techniques available, some will only be mentioned briefly, whereas an extensive coverage will be given to photoelectron spectroscopy. That includes building upon the theory of photoelectron spectroscopy

for anion molecule clusters, the apparatus setup and the basis of the *ab initio* computations.

1.2 Potential energy surface

Before proceeding to the different spectroscopic techniques, it is imperative to realise the significance of a potential energy curve for a diatomic molecule or potential energy surface for a polyatomic molecule. The potential energy surface is defined by the Born-Oppenheimer approximation, where the motion of the nuclei and electron can be treated separately. In this approximation, the energy of the cluster is a function of the position of the nuclei, and the number of electrons in the system.

Consider a topographic map of a landscape with hills and valleys to be the potential energy surface of a cluster, one slice through such a landscape is a potential energy curve projected in Figure 1.
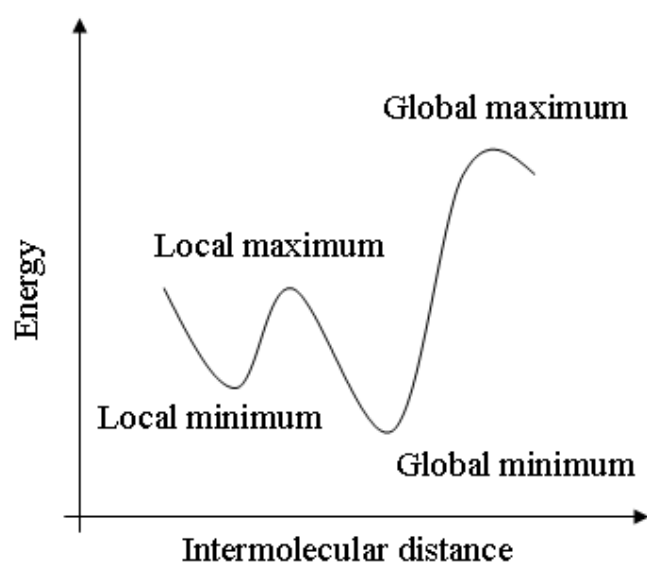
Figure 1. Common points on a 1-D potential energy curve

Zero gradients along the potential energy curve reflect different equilibrium molecular geometries or transition states of the cluster. The most important point is the global minimum. This stationary point, i.e. point with the zero gradient, corresponds to the most stable nuclear configuration. Other stationary points located on this curve, may reflect unstable configurations and hence are maxima. Unlike minima, which have minimum values in all directions (well-like feature); a maximum point may have minimum values in all directions except one which has a maximum value (hill-like feature). This particular

4

point is also known as a first order transition state. As all these stationary points are characterized by a zero gradient, a second derivative of the energy with respect to the nuclear coordinates is required to distinguish them. The second derivative of the function comprises what is commonly known as the Hessian Matrix. For n variables, the matrix is n by n and has n eigenvalues, and a first order transition state is located when one will find that all the eigenvalues are positive except for one.

As bond lengths, bond angles and bond energies are the key information gathered from experiments that probe the ion–molecular interaction they are used to construct, or test the validity, of potential energy surfaces which in turn can be used to predict reaction rates and other dynamical properties. One aspect of this thesis is that potential energy surfaces will be constructed from calculation and that can be used to illustrate geometrical changes that occur within the anion cluster following a transition due to photo excitation and detachment of an electron.

1.3 Spectroscopic techniques

Spectroscopy is principally the study of interaction between radiation and matter. When a molecule is irradiated, the initial process is known as induced absorption, in which after absorbing a microwave, infrared or ultraviolet photon, the molecule will increase its rotational, vibrational or electronic energy. After the absorption process, emission processes may occur either spontaneously or be induced. In the former case, the excited molecule spontaneously emits a photon of radiation which can be described by equation (i).

$$\mathrm{M}^{*} \longrightarrow \mathrm{M} + h\nu \qquad\qquad (i)$$

In the later situation, a second quantum of radiation is required to induce the emission process as given by equation (ii)

$$M^* + h\nu \longrightarrow M + 2h\nu \qquad\qquad (ii)$$

Generally, a spectroscopist is concerned with the absorption or emission of radiation by the atoms or molecules as valuable information can be obtained. In absorption spectroscopy, the intensity of the radiation as a function of wavelength before and after the interaction is measured and compared. In the case of emission spectroscopy, the wavelengths of the radiation emitted by the atom or molecules after interaction will be noted. However, in the spectroscopy of ion-molecule complexes, the amount of complexes present is too low to obtain a significant light attenuation, therefore, relies on another event which follows the absorption, i.e. fragmentation, photodetachment to record a spectrum. Presented in Table 1 are some examples of anion cluster systems that have been spectroscopically characterized by different techniques.

Table 1. Representative anionic complexes studied by different spectroscopic methods

Cluster	Methods of study	Reference
$X^-\ldots H_2$ ($X^- = I^-, Cl^-, Br^-$)	VP, SEVI, PES	10, 11
$X^-\ldots HCCH$ ($X^- = I^-, Cl^-, Br^-$)	VP	10-12
$F^-\ldots CH_4$	VP	13
$I^-\ldots H_2O$	VP, ZEKE	14, 15
$H_2O^+ - Ar$	VP	16
BN^-	PES	17
$BrHBr^-$	VP	18

Abbreviations: VP (Vibrational Predissociation), ZEKE (Zero Kinetic Energy photoelectron spectroscopy), PES (Photoelectron spectroscopy), SEVI (Slow electron velocity-map imaging)

1.3.1 Vibrational predissociation spectroscopy

An example for an event based technique is Vibrational Predissociation (VP) spectroscopy, pioneered by Yuan Lee and co-workers[19] in the 1990s. Photon energies of infrared radiation are not large enough to excite electrons in molecules, but could induce molecular vibrations. The exact frequency at which a vibration occurs is determined by the strength of the bond and the mass of the atoms involved.

Figure 2. Scheme for obtaining a vibrational predissociation spectrum using H-H…Cl⁻ dimer as an example Adapted from reference.[11]
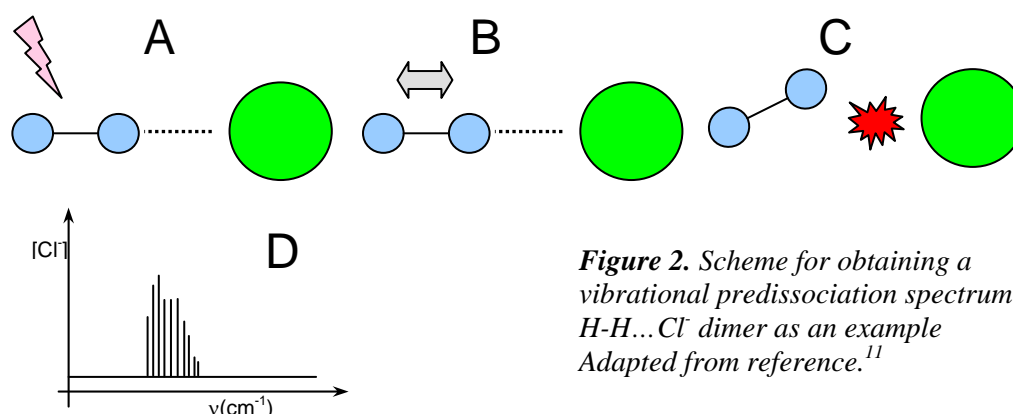
A schematic of VP spectroscopy is illustrated in Figure 2 for the Cl-H_2 dimer. In the step A, infrared radiation induces a high frequency vibration which is just localised on the H–H stretch. In the free H_2 molecule, the H–H stretching vibration is not infrared active however when the H_2 molecule is attached to an anion the H – H stretch becomes infrared active. In VP spectroscopy the energy initially deposited in the H_2 stretch eventually migrates to the weak intermolecular bond causing it to break (step C) Finally, a VP spectrum is yielded by recording the amount of charged Cl⁻ fragments while tuning the infrared wavelength.

1.3.2 Photoelectron spectroscopy

The underlying principle of photoelectron spectroscopy (PES) is based on Einstein's photoelectric effect, and it involves the ejection of electrons from atoms or molecules following bombardment by photons. It is also an event based spectroscopy as

information is obtained from the energy of the ejected electrons. This effect was discovered when the surface of alkali metal was bombarded with photons above the threshold frequency.
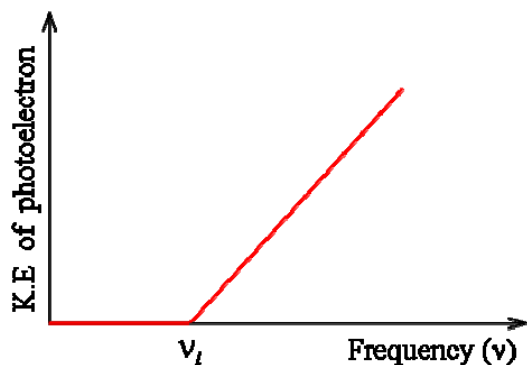
Figure 3. *Variation of kinetic energy of photoelectrons with the frequency of incident radiation. Adapted from reference.[20]*

As illustrated in Figure 3, by increasing the frequency beyond the threshold frequency, v_l the photon has sufficient energy to allow the electron to overcome the binding energy of the electron, i.e. work function of metal. The excess energy of the photons is converted to kinetic energy of the ejected photoelectrons, expressed as

$$hv \ = \ \Phi \ + \ \text{Kinetic Energy} \ = \ \Phi \ + \ \frac{1}{2}m_e v^2 \qquad (4)$$

where Φ is the work function of the metal, m_e and v are the mass and velocity of the photoelectron. This technique, involving the use of high energy photons, can be extended to a gaseous sample and the work function term would then be replaced by the ionization energy of an atom or molecule, hence, equation 4 becomes

$$hv \ = \ \text{Ionization Energy} \ + \ \frac{1}{2}m_e v^2 \qquad (5)$$

In a gas phase measurement, the photon will detach an electron from a particular orbital if it has energy greater than the binding energy of the electron. The excess energy imparted by the photon leaves the molecule in the form of kinetic energy of the ejected electron. Radiation in the far ultra-violet region of the electromagnetic spectrum is commonly used in photoelectron spectroscopy as it has sufficient energy

to detach the valence electrons of atoms or molecules. The electrons from the valence shell are those involved in chemical bonding. They have a characteristic binding energy which corresponds to their orbital and these characteristics are reflected through their kinetic energy when detached. Since the square of velocity is proportional to energy, the time-of-flight of a photoelectron from its formation to detection is a good measure of its kinetic energy.

This relationship is given

$$\text{K.E.} = \frac{1}{2}m_e v^2 \tag{6}$$

$$v \propto \sqrt{2\ \text{K.E.}} \tag{6a}$$

where m_e is the mass of electron and v is the velocity. Figure 4 shows an ideal photoionization process and the photoelectron spectrum of an atom. The spectrum on the inset is a record of the number of electrons detected at different energies with respect to their orbital.
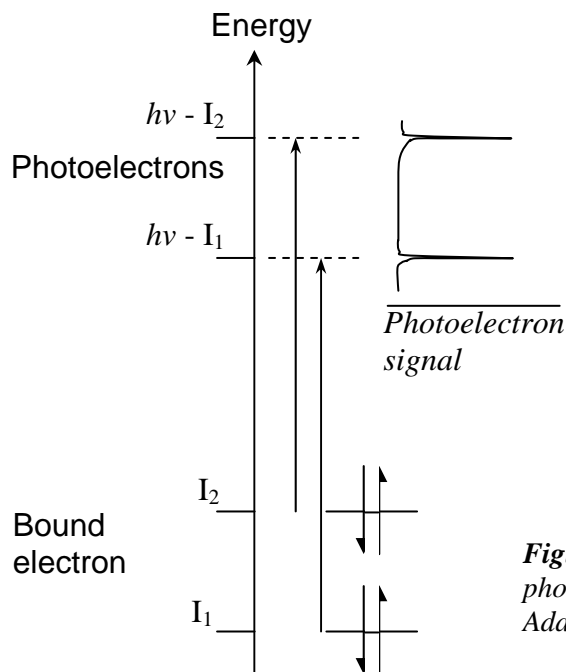
Figure 4. Ideal photoionization process and photoelectron spectrum(inset) Adapted from reference.[21]

1.4 Anion photoelectron spectroscopy

Anion photoelectron spectroscopy operates in an identical fashion as to the conventional photoelectron spectroscopy of neutral species. Photoelectron spectroscopy of neutral molecules yields information on cationic energy level from a cation $\leftarrow$ neutral transition, whereas anion photoelectron spectroscopy involves neutral $\leftarrow$ anion transitions and that allows the study of neutral molecular states. Another attractive feature when conducting experiments with anions is the ability to carry out mass selection prior to spectroscopy. This mass selectivity freedom allows one to venture into studies involving clusters of higher orders, i.e. $X^-...[HA]_n$ where $n>1$.

As shown in Figure. 5, the absorption of ultraviolet radiation by the anion-molecule complex results in the ejection of an electron leaving a neutral complex. The kinetic energy of the ejected electron is then measured to allow the construction of potential energy curves as depicted in Figure 6.
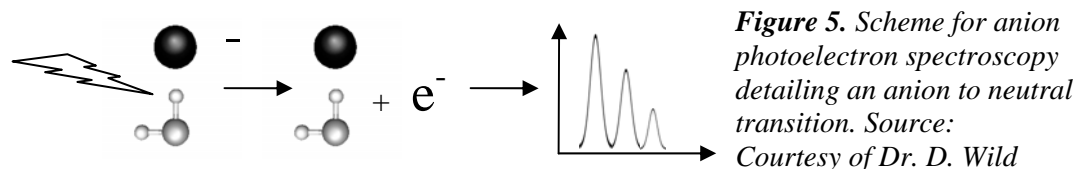
Figure 5. Scheme for anion photoelectron spectroscopy detailing an anion to neutral transition. Source: Courtesy of Dr. D. Wild

Figure 6 shows the potential energy curves that describe the intermolecular interaction between the anion and neutral molecules (X^- + HA) and the corresponding neutral–neutral intermolecular interaction (X + HA).
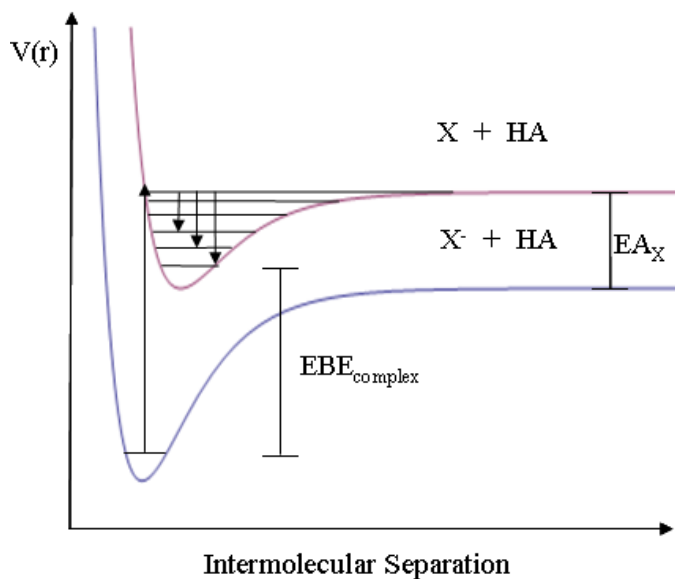
Figure 6. *Potential energy curves describing the anionic cluster with its corresponding neutral cluster detailing electron affinity and electron binding energy.*
Source: Courtesy of Dr. D. Wild.

The transition from a lower energy anion surface to the neutral surface due to absorption of ultraviolet light is indicated by the vertical upwards arrow and energies of the ejected photoelectrons as reflected by the vertical down arrows, and are determined by the energy levels of the neutral complex. The transition back to the ground vibrational state of the neutral complex is indicated by the longest downward arrow, this also corresponds to the photoelectron with the highest kinetic energy. One can determine the electron binding energy, termed as EBE $_{complex}$ in Figure 6 from the energy difference between the UV radiation and the largest transition in the neutral state. The electron affinity (EA_x) of the anion X^- is generally already known, however if not it can be found by recording the photoelectron spectrum of the bare anion.

1.4.1 Apparatus setup

A Time of Flight Mass Spectrometer in tandem with a Photoelectron Spectrometer (TOF-PES) has been constructed for the planned anion photoelectron spectroscopy experiments. Each individual component that forms this home built instrument and its function will be introduced. Figure 7 shows the schematic diagram of the TOF-PES in the laboratory.

It is assembled from seven stainless steel chambers and divided into two regions by the gate valve as depicted. The source and extraction chamber, which are positioned before the gate valve are maintained at a vacuum of 10^{-8} torr, by two diffusion pumps and a cryo-trap. The remainder of the chambers on the other side of the gate valve are evacuated by two turbomolecular pumps and attain a lower pressure of 10^{-9} torr. It should be noted that rotary pumps are also installed in this vacuum system. They are used to evacuate the chambers as a first stage towards high vacuum and they also serve to remove the throughput from the diffusion and turbomolecular pumps.

Photoelectron
Flight Tube

Mass gate and Deceleration

Gate Valve

Deflection plates

Extraction plates

Extraction Chamber

Ion Detection
Chamber

Laser Interaction
Chamber

Einzel Lens Chambers
ConFlat

Conical skimmer

Gas nozzle

Source Chamber
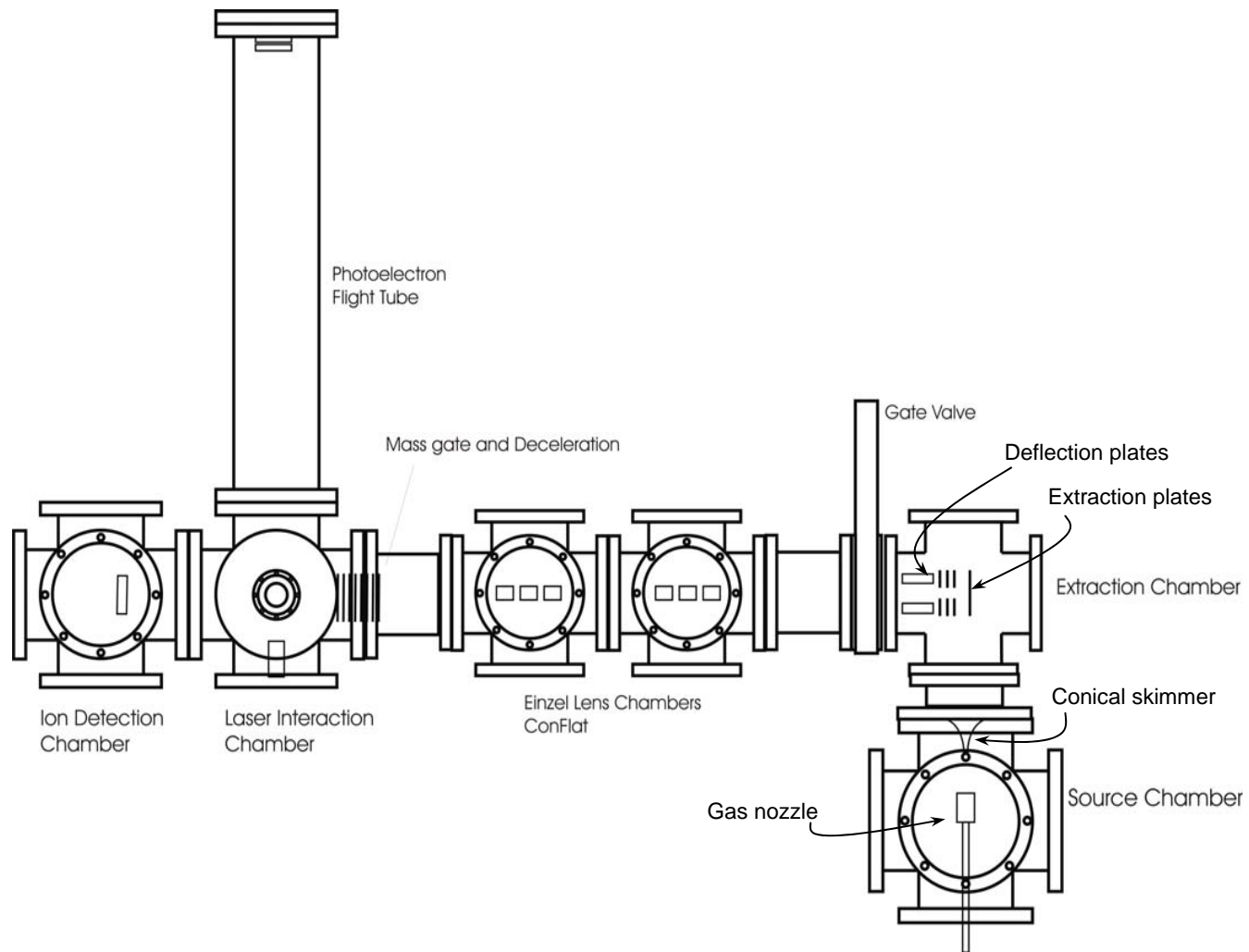
Figure 7. *Schematic diagram of the TOF-PES in the laboratory*

Another important component that is presented in Figure 8 is the Gas Mixing Station (GMS). This is the starting point prior to any experiment performed in the TOF-PES, as illustrated; the GMS have four inlets and two outlets. Gaseous samples can be introduced via A, B and C directly from gas bottles while the sample vial can be used to hold a volatile liquid and allow the vapour to enter via gas line D. After achieving the correct ratio, the gaseous mixture can be sent to the source chamber.
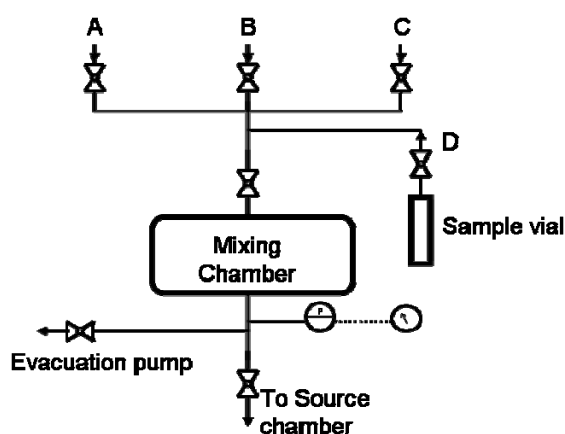
Figure 8. Schematic diagram of the gas mixing station

The basic operation of a TOF-PES can be summarised in four steps: (i) ion and ion-cluster generation, (ii) mass separation of anion clusters, (iii) photodetachment of electrons with a UV-light source and finally (iv) analysis of the energies of the ejected electron.

The production of negative ions occurs in the source chamber, where the gas mixture from the GMS is delivered via a gas nozzle pulsing at 10 Hz. The gas mixture expands adiabatically into the high vacuum and undergoes dissociative attachment of electrons produced from thermionic emission from rhenium filaments to form the negative ion clusters. Subsequently, the negative ion clusters en route to the extraction chamber are shaped into a collimated molecular beam by a conical skimmer to facilitate the extraction of ions from a well defined volume.

When the pulsed molecular beam arrives at the centre of the extraction chamber, large negative voltages are pulsed to the ejection plates and the ions are deflected (towards the left on Figure 2) into the Wiley-McLaren type[22] time of flight mass spectrometer. Mass separation is an important prerequisite in this particular experiment and the principle behind time of flight mass spectrometry can be understood from the relationship between velocity and mass expressed as;

$$v \propto \sqrt{\frac{1}{m}} \qquad (7)$$

Here, v is the velocity of ions which can be determined from the length of the flight tube and time of flight and m is the mass of the ion. As all the ions enter the mass spectrometer with the same kinetic energy, the velocity of the ions and hence their time of flight is dependent on their mass.

Considering that the path of the molecular beam is deflected sharply at right angle from its original trajectory and due to the fact that all ions have a negative charge, the subsequent components are meant for beam guidance. Coupled onto the rear of the ejection plates are two pairs of ion deflection plates positioned parallel to the molecular beam. Their purpose is to steer the beam and align it through the apertures of the time of flight tube. Finally, there are two sets of Einzel lens chambers mounted in series, which are used to focus the beam and negate the coulombic repulsion experienced between the like charged ions.

Just before the laser interaction chamber, the ions will transit through another series of electro-optics, referred to as the mass gate and ion decelerator. These components improve the mass selection capability and reduce the speed of the charged beam. This latter feature reduces Doppler broadening and therefore enhances the resolution of the

recorded photoelectron spectrum. The mass gate is a lens charged at a high negative potential that impedes the anionic beam, however, it can be pulsed to ground potential for a short period, allowing the passage of certain mass selected clusters. During this short window of time offered by the mass gate, the ion decelerator which is made up of seven plates is pulsed to a low negative potential with the intent of slowing down the charged clusters.

The ions are now in the region where photoelectron spectroscopy takes place. An overview of the photodetachment process and the respective components of the photoelectron spectrometer is summarised in Figure 9.
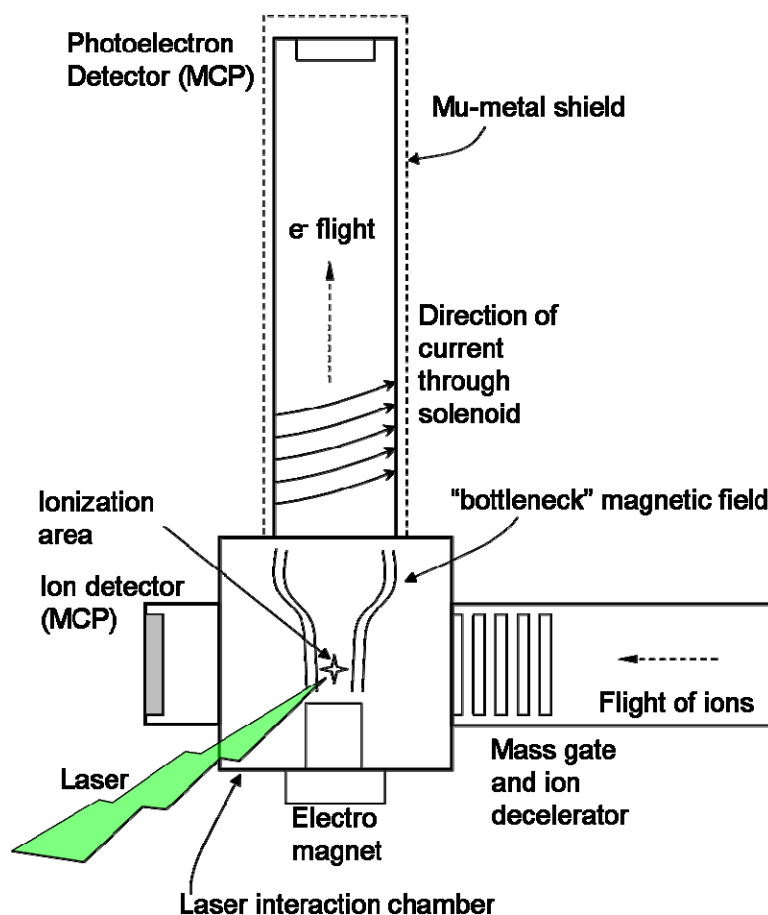
Figure 9. *Schematic diagram on the photoelectron spectrometer*
with apparatus to guide and detect photoelectron

The first step of photoelectron spectroscopy is interaction of the ion cluster with the fourth harmonic of a Nd:YAG laser (266 nm). By synchronising the timing (see

Materials and Methods) between the pulsing of the extraction plates and the firing of laser, photodetachment can be carried out on mass-selected clusters based on their time of flight.

Photoelectrons are gathered by a unique magnetic field, created by coupling the magnetic fields of a ferromagnet and solenoid. When current is passed through the solenoid wound around the photoelectron flight tube, a weak magnetic field parallel to the flight tube is generated. The upstream of the solenoid magnetic field is coupled to the magnetic field of a ferromagnet, which creates a "bottleneck".[8] This ensures that upon photodetachment of the anion, the electrons released will traverse a common path into the photoelectron flight tube as illustrated in Figure 10.
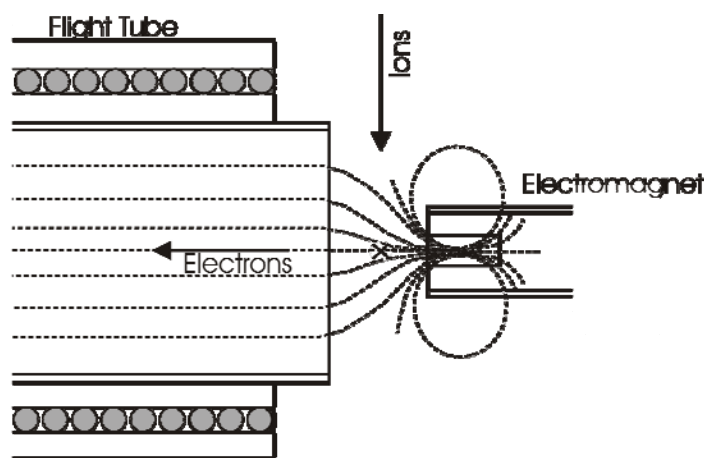
Figure 10. The coupling magnetic field of the electromagnet and solenoid wound around the flight tube produces a "bottleneck" field Source: Courtesy of Dr. D. Wild

In addition to the guidance provided the magnetic field, the photoelectron flight tube it is protected by a mu-metal (μ-metal) tube. This μ-metal shielding tube is made from nickel-iron alloy and has high magnetic permeability property. Hence, interferences to the photoelectron flight path are eliminated by "attracting" earth magnetic field into the μ-metal tube, creating a path around the shielded area.

1.4.2 Ion and electron detection

The photoelectrons are detected with a microchannel plate (MCP) mounted onto the terminus flange. The MCP is made up of an array of electron multipliers fabricated onto a glass plate. The electron multiplier channels are arranged parallel to one another can be oriented normal to the surface of the plate or biased at a small angle. The mode of operation can be pictured in Figure 11, where a single primary particle is shown entering the channel, which sets off a cascade of secondary electrons.

This detection of signal relies on the secondary electron emission which occurs in the channel multiplier. Performance is a function of the ratio l/d, where l and d is the length and diameter of the channel. Straight channel multipliers normally achieve a gain of $10^3 - 10^5$ and this limitation is due to the onset of ion feedback.[23] A common method to increase the gain and suppress ion feedback is the chevron arrangement, where the plates are oriented that the channels are angled typically at $8^o/8^o$ or $0^o/15^o$.
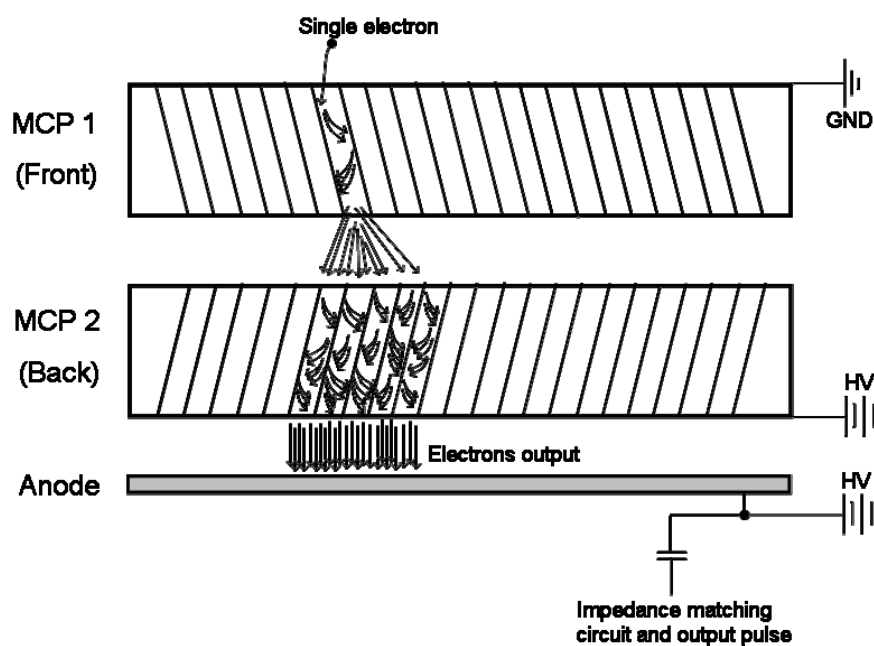
Figure 11. Schematic of a chevron microchannel plate in operation.

1.5 Additional photoelectron spectroscopy techniques

It should be noted that anion photoelectron spectroscopy, which is the central technique of this thesis is not perfect. The current apparatus setup is a basic configuration; however, it is possible to upgrade it. The intention of this section is to highlight two additional photoelectron spectroscopy techniques. These advanced variants employ tunable lasers and have more sophisticated photoelectron detection schemes.

1.5.1 Threshold photodetachment spectroscopy

Threshold photodetachment spectroscopy, also known as Zero Kinetic Energy photoelectron spectroscopy (ZEKE) is a variant of photoelectron spectroscopy technique. The principle of ZEKE spectroscopy is based on photodetachment of electron near the threshold level using a tunable laser, thus producing photoelectrons with almost zero kinetic energy. This method of photodetachment combined with a delayed detection scheme (illustrated in Figure 12.) adapted from the design of Muller-Dethlefs[24] is able to improve the resolution significantly.
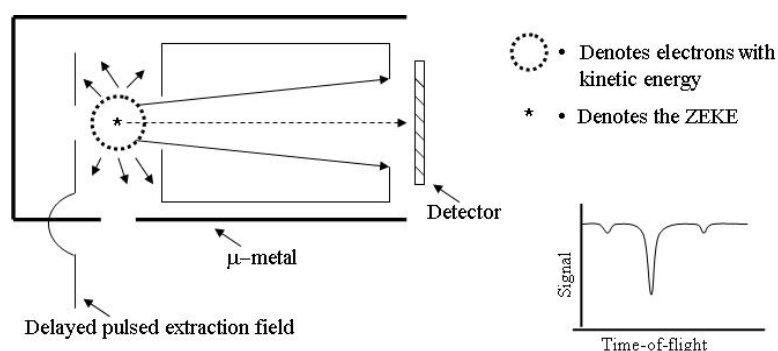
Figure 12. *Schematic for detection of ZEKE electrons and the signal output (inset). Adapted from reference.[24]*

Consider the formation of zero kinetic energy electrons and those with appreciable kinetic energy under field free conditions. After a suitable time delay of 100 nanoseconds for example, electrons with non zero kinetic energy will disperse as

shown in the diagram, while those electrons with zero kinetic energy will have stayed at the point of electron detachment (marked by the asterisk).

When the extraction pulse is applied, the dispersed electrons will be accelerated to different energies and therefore feature different flight paths compared with the zero kinetic energy electrons, which will transverse down the time-of-flight tube reaching the detector as shown by the dotted arrow. The discrimination against electrons with larger kinetic energy was achieved as shown by the insert of the output signal on Figure 12. The spectrum displayed a strong peak for ZEKE due to the higher intensity of electron received by the detector while the electrons with kinetic energy being projected off-axis generate a low signal.

An illustration of the high-resolution capability of ZEKE spectroscopy is given in Figure 13. The photoelectron spectrum of iodide anions with carbon dioxide molecules was taken using a tunable light source by Neumark and co-workers.[25] A resolution of 10.0 meV is superimposed on their ZEKE spectrum, with the latter technique achieving a resolution of 1.0 meV. Finer structure is observed with ZEKE spectra revealing sub bands.

Figure 13. ZEKE spectrum (solid lines) and photoelectron spectrum (dotted lines) of $I^-...[CO_2]$. Taken from reference.[25]

1.5.2 Slow electron velocity-map imaging

Following the development of ZEKE, another variant of the photoelectron spectroscopy has been developed. Neumark and co-workers pioneered this technique called slow electron velocity-map imaging (SEVI)[26] in response to the shortcomings of ZEKE spectroscopy. The acquisition time for an anion ZEKE spectrum is much longer compared to conventional photoelectron spectroscopy as the laser is scanned at small increment and the near-zero electrons produced are very sensitive to stray electric and magnetic fields. In addition to the experimental difficulties, ZEKE has restricted applicability due to the Wigner threshold law and one is limited to investigation of species where the electron leaves as an *s* wave.

SEVI can be classified as a composite of the conventional photoelectron spectroscopy and zero kinetic energy photoelectron spectroscopy. Using a tunable laser, the energy levels were scanned in small steps as shown by the grey areas on Figure. 14 instead of each individual level employed in the ZEKE scheme.

Figure 14. Schemes of excitation for
a) conventional photoelectron spectroscopy
b) anion zero kinetic energy spectroscopy
c) slow electron velocity map imaging
Taken from reference[26]

The experimental arrangement for this scheme is similar to its predecessor. Here, photodetachment of anions are carried out in an environment with a DC electric field which projects the photoelectron velocity distribution onto a detector coupled to a phosphor screen. The final outcome shows that this variant of photoelectron

spectroscopy is able to overcome some of the problems encountered in ZEKE spectroscopy and produce results of similar resolution in a shorter acquisition time.

1.6 Theoretical methods

Advances in experimental technologies and spectroscopic methods have been tremendous in the past few decades, allowing spectroscopists to make more accurate measurements and explore more exotic types of complexes. In addition, a theoretical investigation of ion – molecule interactions by computer modelling is another field of study that has been playing a critical role. Quantum chemical calculations, which were often incorporated with experimental work, are mainly used to provide predictions for various spectroscopic properties or assist with the assignments and interpretations of experimental data.

The initial step towards modelling is usually computation of the energy of a molecule for a specific nuclear configuration, governed by the Born-Oppenheimer approximation. An "estimated" nuclear geometry is used and the energy is calculated, this computation cycle is repeated until the equilibrium geometry is obtained. The methods used can generally be classified into three divisions, molecular mechanics methods, *ab initio* methods and semi-empirical methods. The former uses classical mechanics and empirical force fields to describe the energy while the latter two involved solving the approximate Schrödinger equation for the system. These theoretical methods are fundamentally different but their application can be used in close affiliation. For example, *ab initio* methods which use only the fundamental physical constant empirical parameters can employ molecular mechanics to obtain an approximated nuclear geometry to be use as a starting point. On the other hand,

parameters calculated from high-level quantum computation can be use in molecular mechanics calculations to improve the quality of approximation.

The theoretical work described in this thesis draws upon simple ion – molecule interactions and largely electronic transitions. Therefore, theoretical computations, where the Schrödinger equation is solved with Born-Oppenheimer approximation are most appropriate.

There are a number of programmes for *ab initio* computations and two of the common ones are GAUSSIAN 03[27] and GAMESS [28]. These programmes are used routinely for geometry optimisations and for producing potential energy surfaces. The levels of theory and basis sets used for the calculations are determined depending on the molecular system studied and the degree of accuracy intended.

2. Material and Methods

2.1 Experimental Aspects

As with any purpose built instrument, the next logical stage after construction is the testing phase. Considering the nature of this instrument, where a time-of-flight mass spectrometer is coupled to a photoelectron spectrometer, it is critical that a well resolved mass separation should be achieved before undertaking any photoelectron experiments. Thus, the majority of the optimisation efforts focus on the enhancement of the mass resolution. However, it would be an unrealistic task to strive for a perfect spectrum so these optimisation efforts only aim to produce spectra with reasonable signal to noise ratio and resolution, allowing quality information to be obtained. For the ease of understanding, the following discussion on the material and methods of instrument testing and modifications are listed with respect to their chronological order as experienced by the anions in the beam.

2.1.1 Gas mixing station

A fundamental gas-phase photoelectron experiment for probing an ion – molecule species would require at least three different compounds, namely, the buffer gas, neutral molecule and the anion precursor. It is essential for the gases to be mixed accurately and diluted with the appropriate amount of buffer gas before sending it to the source chamber. For this reason, a pressure gauge [29] was acquired, and needed to be calibrated. The top circuit diagram given in Figure 15 is designed to step down the mains voltage and provide regulated +5 and -5 volt supplies, used to power the pressure gauge and the electronics for calibration. The bottom inset on Figure 15 is a circuit designed to achieve linear amplification of the gauge output. The main components are the general purpose operation amplifier (op-amp) with three variable resistors. Calibration begins by offsetting the pressure gauge to register zero volts for

24

an evacuated chamber (with R3) and later increased the gain to one volt (with R1) for a chamber with 100 psi of pressure. This iterative procedure can be concluded when the readings on the LCD is responding linearly to display 0 to 100 psi.
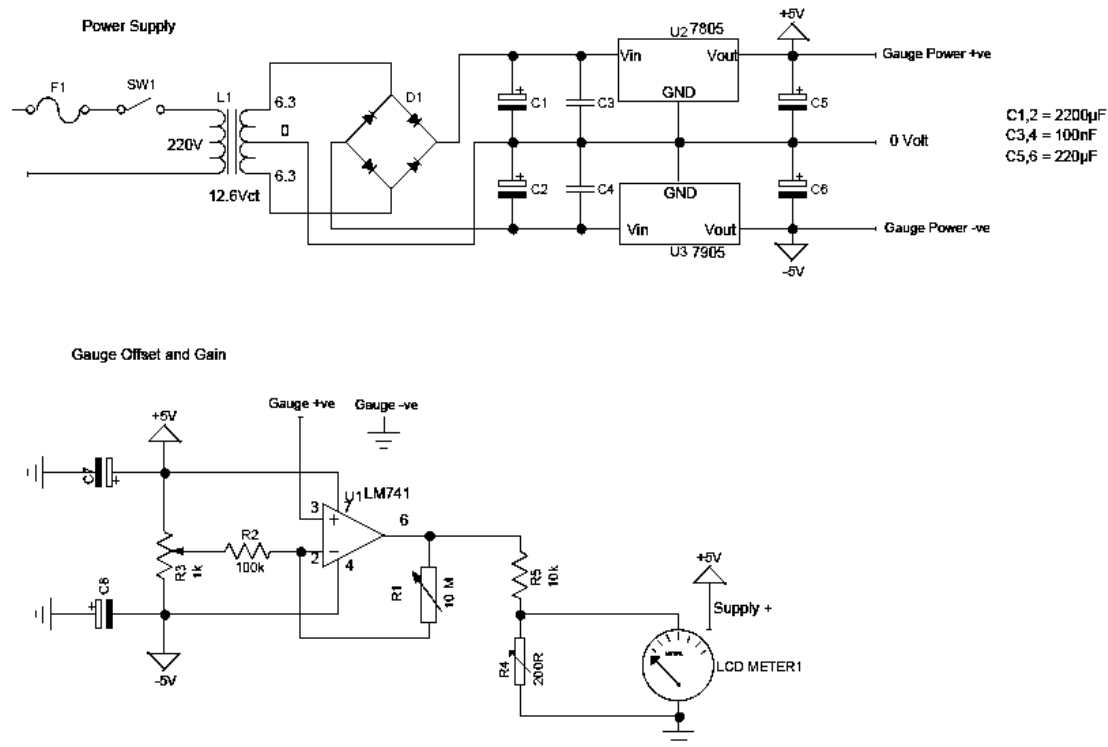
Figure 15. Circuit diagram for pressure gauge calibration

2.1.2 Optimisation of anion cluster formation

Since the source chamber is where the formation of anionic cluster/complexes occurs and the beginning of the molecular beam, one of the earlier efforts to improve the signal of the time-of-flight mass spectrometer is to increase the radial dimension of the molecular beam. The original conical skimmer had a 1 mm diameter orifice was replaced with a 3 mm skimmer and this was a very significant change when comparing in terms of molecular sizes. Quantitatively, the flux of gas clusters would be increased by a factor of nine.

Low energy electrons are essential for the formation of anionic cluster/complex, however, a large amount is not desirable as it will contribute to show background electrons and saturate the detectors. A significant upgrade towards the stability of anionic cluster/complex formation and minimisation of stray electrons is the acquisition of a regulated current supply (0-5 A) and a pulsed negative voltage supply[30] (0-300 V, width 0-999 μs). These two power supplies are connected as illustrated in Figure 16 to afford stable and sharp pulses of high voltage to the twin Rhenium filaments. A constant voltage would imply a steady thermionic emission of electrons and the pulse function is used to regulate the amount of electrons produced, and ultimately to time the electron burst to coincide with the gas pulse.
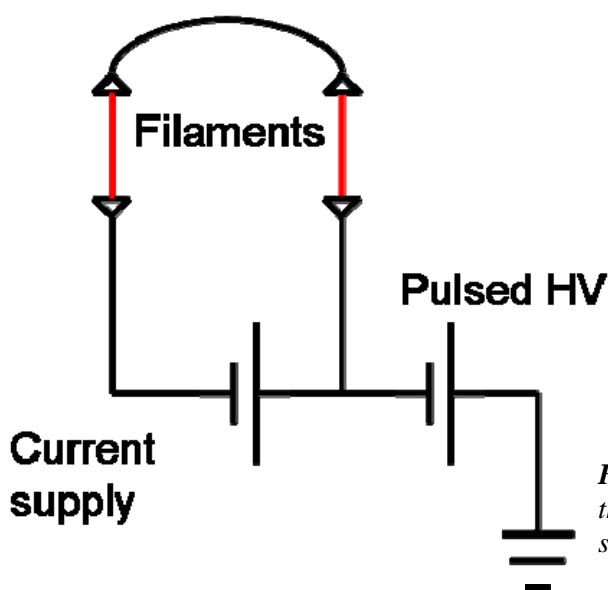
Figure 16. *Schematic diagram of the power supply for electron supply filaments*

Another attempt to reduce the stray electrons was the installation of a wire mesh nestled around the source assembly plate, forming a shield of ground potential. Another enhancement was to coat the entire source assembly including, the structural supports, the wire mesh and the conical skimmer with a layer of conductive graphite. This creates a ground potential and prevents any charge build up, which would deflect the ions and electrons.

2.1.3 Optimisation of ion deflection in the extraction region

As mentioned previously, the molecular beam needs to be guided to the detector to maximise detection. The previous design of the ion deflection system is given on the left of Figure 17. It consists of four plates arranged parallel to the beam, where guidance along y-axis and x-axis can be controlled with plates 1, 3 and 2, 4 respectively. An adjustable power supply of ± 100 volts is applied to each plate to steer the ions and align them through the entrance aperture of the TOF tube. At a constant voltage, the magnitude of electric field will increase accordingly to the inverse square law as the distance between two charged parallel plates decreases, given as;

$$\frac{E_1}{E_2} = \frac{(d_2)^2}{(d_1)^2} \tag{8}$$

where E_1 and E_2 are the magnitude of electric field at respective distances, d_1 and d_2. The aim of this modification is to increase the effect of the xy-deflection plates by bringing them closer to the anion beam. A simple solution to this without having to remove the original internal structure was shown on the right schematic of Figure 17. Four pieces of square brass tube were fixed onto the original plates and hence decreased the distance between the plates and the ion beam by 12.7 mm.
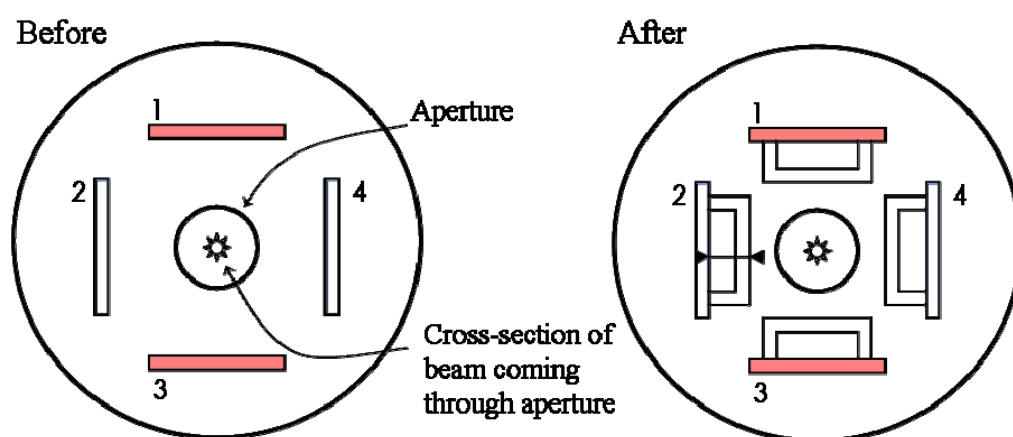
Figure 17. *Schematic drawings of the xy-deflection plates before and after modification.*

2.1.4 Optimisation of ion and electron detection

From the introductory chapters, the gain of microchannel plate (MCP) detectors is known to be very high; therefore, it is important to avoid saturating the detectors in order to obtain the entire spectrum. Observation and recording of the mass spectrum is achieved by the use of an oscilloscope and this leads to another problem, the high impedance output from the MCP will not be well matched to the low impedance of the oscilloscope. This problem was overcome by an impedance matching circuit [31] connected to the anode of the MCP. The details of the circuit are shown in Figure 18 with Figure 11 inserted.
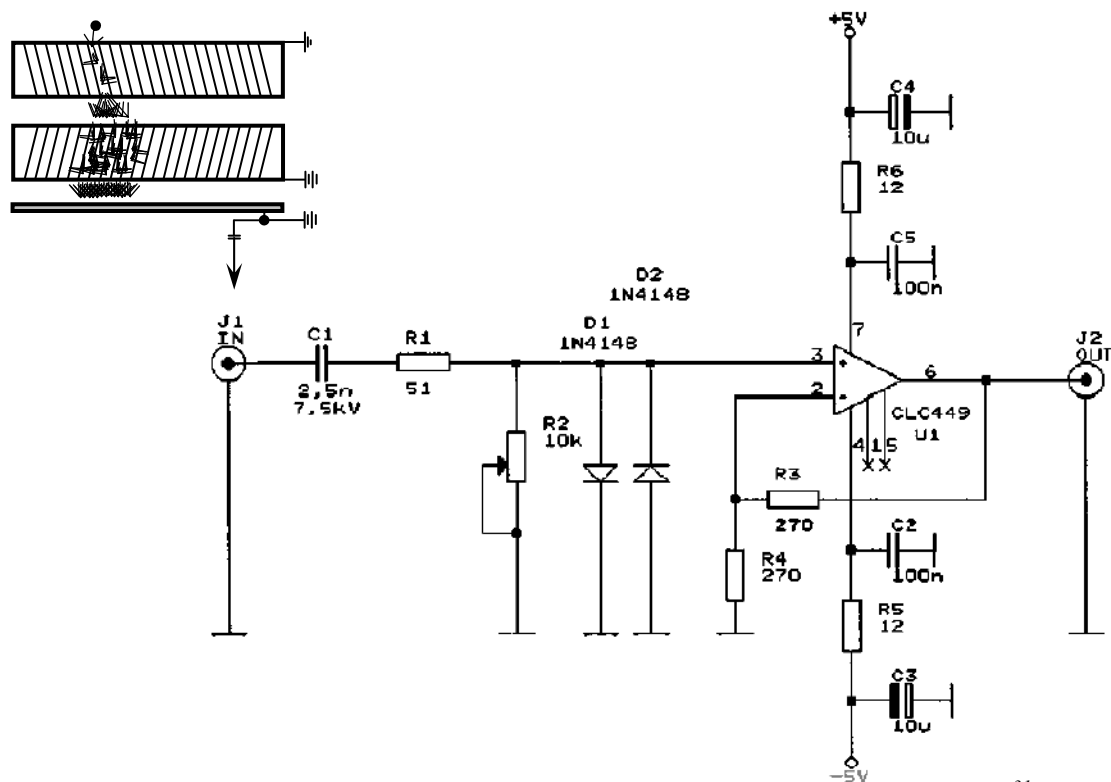
Figure 18. *Impedance matching circuit on the anode of MCP. Taken from reference.[31] Inset from Figure.11*

The component labelled U1 in Figure 18 is the critical component of this circuit. This monolithic op-amp works with high input impedance and gives an output of low impedance is used as a non-inverting amplifier to match the impedance between the MCP and oscilloscope.

2.1.5 Safety system of the apparatus

High vacuum conditions are important in molecular beam experiments however to achieve such conditions, it requires substantial pre-evacuation and other efforts. For this reason, the vacuum pumps operate constantly to maintain high vacuum in the chambers of the TOF-PES even when no experiments are being carried out. Hence, to preserve the vacuum integrity and to protect the chambers against contamination in an event of pump failure due to power stoppage or cooling water deficiency, a safety system has been developed.

In general, the outputs of the pressure gauges, water flow and heat sensors are monitored constantly and that reflect the state of the apparatus. This entire operation is controlled by two programmable microchips (PICAXE) and BASIC programming code.[32] A simple representation of the programme is given in Figure 19. Although this programme is designed to monitor both the turbomolecular pumps and diffusion pumps, it has the flexibility of doing this independently in the event of failure of either type of pump. For example, the dotted line that linked "Diffoff" to "Turbcheck" illustrates that while the diffusion pumps are down, the turbomolecular pumps are still being monitored and vice versa. However, if that opposite region does fail at this time, an "Alloff" routine will be invoked.
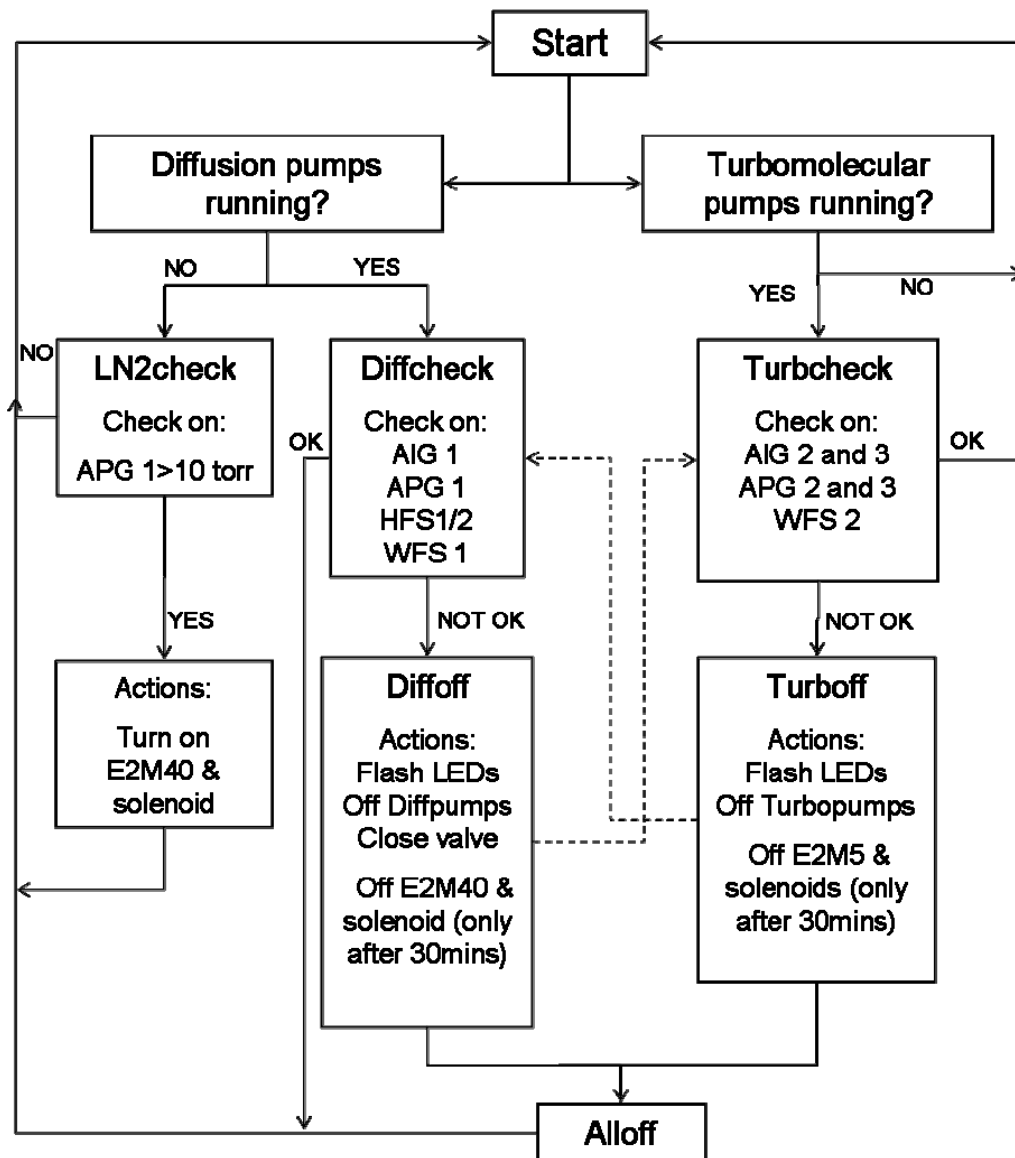
Figure 19. *Overview of the system monitoring programme loops*

To improve the system's monitoring efficiency for better protection, the software has gone through several revisions. One notable change is the implementation of a monitoring routine "Channelread". This revised routine checks the output of the gauges and sensors over an interval instead of every second; hence momentary water flow fluctuations which are the primary concern will not cause unnecessary shut down. After some trial with simulated water flow stoppage, the monitoring period for "Channelread" is set at one minute and for a fault to be registered on the system, the water flow downtime must occur for thirty seconds and more.

The current programme code (revision 7) includes a new routine, "LiqN2check". This loop will be activated when the diffusion pumps are down by monitoring the pressure of Active Pirani Gauge 1 (APG 1), which is located on the backing line of the diffusion pumps. As the name of this routine suggest, when the liquid nitrogen in the cryo-trap empties, the pressure reading on APG 1 will rise. Therefore, starting the E2M40 rotary pump and opening the solenoid will remove the condensate as it boils off, preventing a dramatic rise in pressure which is detrimental to the pressure gauges.

Needless to say, the hardware of the safety system was modified in order to be compatible with the new software. From previous hardware, which only allows one to control the diffusion pumps and monitor the water flow, the new system oversees everything including the turbomolecular pump and the electronics for different components running the TOF-PES. A schematic of the front control panel is given in Figure 20.

Figure 20. *Schematic drawing of the safety system control panel. "By-pass" switches for the respective gauges and sensors on the left and power switches for the pumps, valves and electronics on the right.*

The new safety system now has additional functions. Other then the usual monitoring task, the operations of all the pumps, pneumatic valves and the power supplies to the rest of the electronics can be controlled with their switches on the right hand side of the control panel.

A new feature is the "by-pass" function. The user can choose to overlook any irregularities in the operating parameters that may occur during experiments or carrying out troubleshooting. This convenient solution temporarily overrides the monitoring programme of the specified parameters by switching on their respective by-pass switches on the left hand side of the control panel.

Apart from the high vacuum chambers and potential electrical hazards, the laser used for photodetachment also requires a dependable safety system. Presently, the laboratory is equipped with Laser Interlock System LASERMET ICS-1. This system employs a beam block to contain the laser beam when the laser interlock is tripped, for example, if the entrance to the laboratory is opened without authorisation, the unaware trespasser will be protected from any radiation exposure. The advantage of having this feature is that the operation of the laser itself will not be interrupted and the experiment can continue without the need to restart the entire laser system.

2.1.6 Laser

Radiation of 266 nm (4.66 eV) is required for photodetachment. This light source is obtained by frequency quadrupling a 1064 nm neodymium-doped yttrium aluminum garnet (Nd:YAG) laser. The quadrupling process and arrangement of optics that guide the laser beam to the laser interaction chamber when viewed from the top is illustrated in Figure 21.
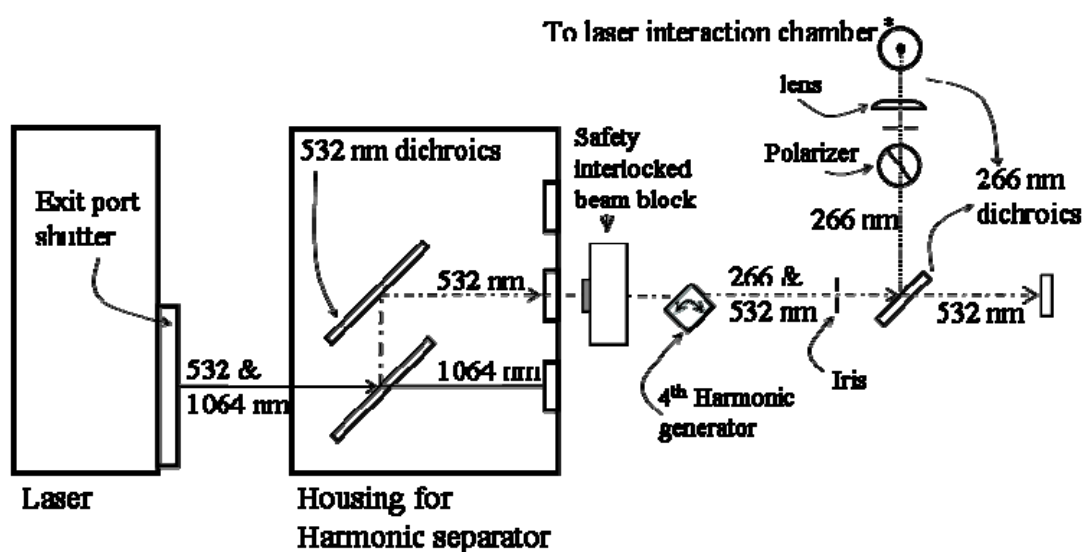
Note: * actual path of laser at this position is coming out of the page

Figure 21. *Schematic diagram of laser bench from top view*

The 532 nm radiation is produced is frequency doubling the fundamental 1064 nm beam by using a second harmonic generator housed within the laser compartment. The beam is reflected by a pair of 532 nm dichroic mirrors, where the 1064 nm component will be filtered and dumped onto a beam block while the 532 nm light continues to the fourth harmonic generator. The 532 nm wavelength is frequency doubled to 266 nm by a β-barium borate (BBO) crystal.

A pair of 266 nm dichroic mirrors is used for re-direction of the beam; the first mirror bends the beam at 90° towards the laser interaction chamber and the second mirror reflects it vertically upward as shown in Figure 21. As for the 532 nm, it will be

directed into the beam blocks as the beam passes through the 266 dichroics. With a series of adjustable iris, the final wavelength of 266 nm laser is narrowed down to afford a well defined beam with minimum stray radiation which is allowed to pass into the chamber. Between the pair of dichroic mirrors, a half-wave plate and a 1 m focal length lens are positioned to change the polarisation and to focus the beam in the centre of the chamber.

The angle of polarisation of the photodetachment laser beam has been shown to affect the angular distribution of the ejected photoelectron and this initial ejection trajectory can affect the detection efficiency.[33] From previous studies by Neumark and co-workers,[34] at $\theta = 0^o$ the angle is parallel to the direction of photoelectron collection, the peaks of the photoelectron spectra are much more intense and better resolved as compared to the perpendicular orientation ($\theta = 90^o$). The angle of polarisation can be understood from Figure 22.
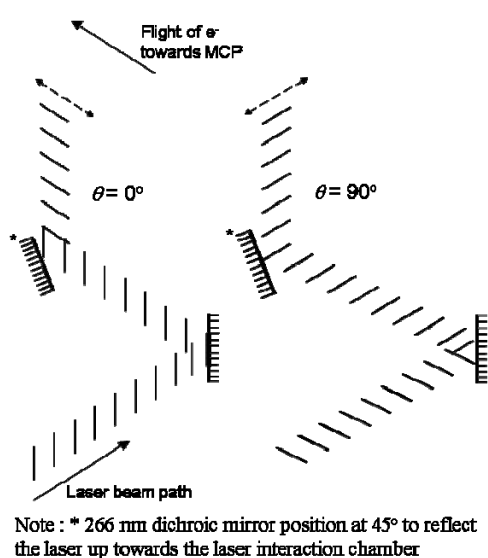
Figure 22. Schematic description of the angle of polarisaiton

While the laser beam has been focused and narrowed down externally to the apparatus, upon entry to the laser interaction chamber, additional graphite coated light baffles are positioned at the entrance port to provide a matt-black surface which reduce the reflection of stray light further. The light baffles which are made of stainless steel coated with graphite have a work function of around 5 eV.[35] These values are larger than the energy provided by the laser and hence stray photoelectrons

will not be produced. On the exit port, a quartz exit mirror tilted at 30° with a second set of light baffle is in place to prevent any reflection of light directly back into the chamber.

2.1.7 Mode of operation, pulsing scheme

Various components of the instrument have been covered in the introductory section and the discussion on the experimental aspect so far has covered most of the modification work that has been carried out. As "time-of-flight" is a critical aspect of this experiment, it is important to again note that the experiment is pulsed at 10 Hz repetition rate and this section covers the essentials of the entire operation with respect to a qualitative description of the timing sequence, Figure 23.

This pulse timing scheme is coordinated by two Stanford Research System digital delay generators (DG 535), where one is assigned as the master control and the other as the slave. As well as controlling the slave delay generator, the master generator is also in charge of firing the laser and pulsing of the electromagnet. The rest of the equipment including the gas nozzle, electron filaments, time-of-flight plates, mass gate and ion decelerator are controlled by the slave delay generator. It should be noted that in this arrangement, the electrostatic lenses do not require timing control, i.e. their fields are static.

At time zero (t_o), a command is given to initiate the timing sequence for the slave timing box. Starting with the gas nozzle, Figure 23 illustrates a cycle of the timing sequence that follows a single gas pulse at t_o.
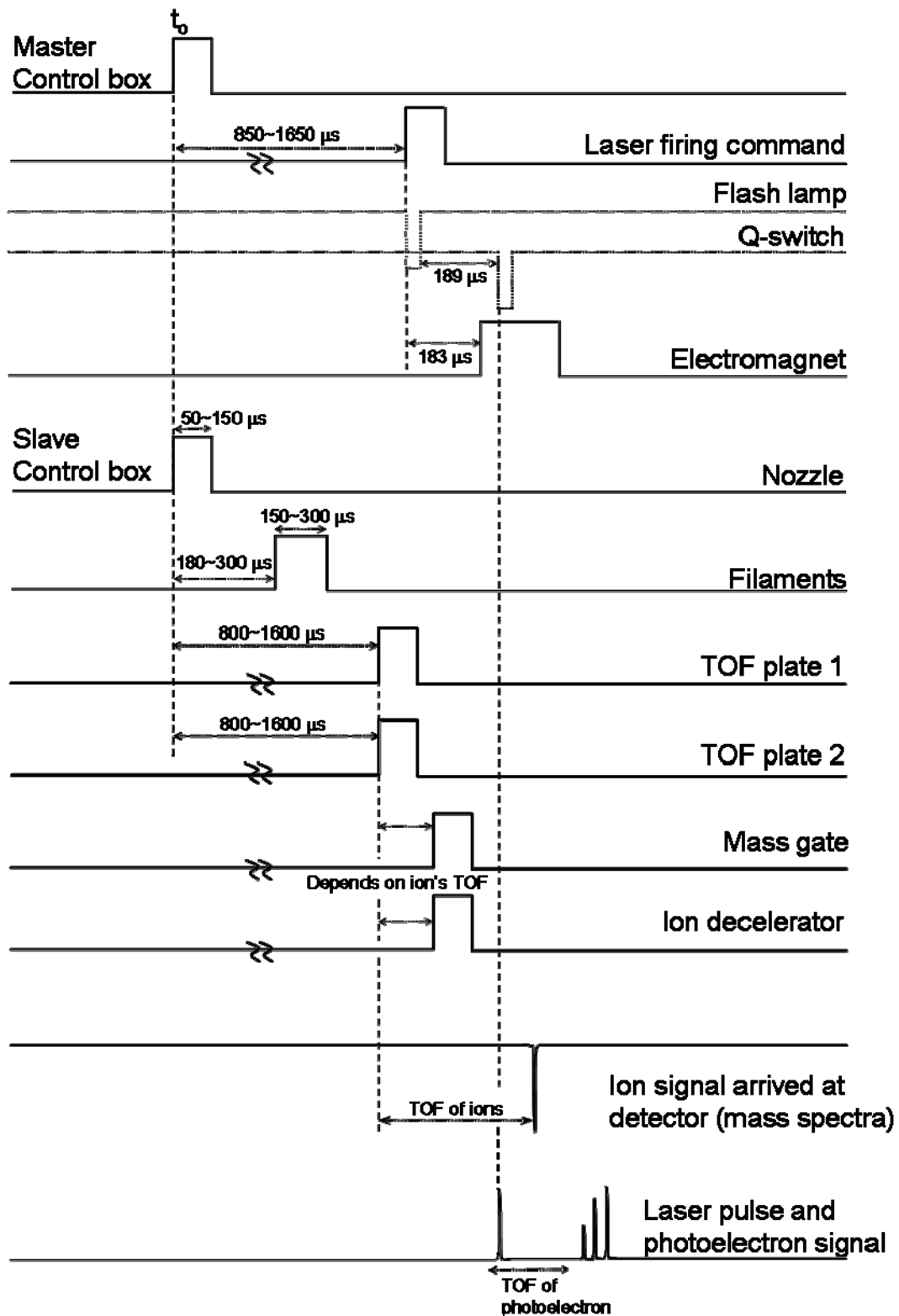
Figure 23. Pulsing sequence for the operation of the TOF-PES

At 150 – 300 μs after t_o, the high voltage supply for the electron filaments is pulsed to produce electrons for the formation of anionic clusters. After production, the anion clusters are extracted for time-of-flight mass spectrometry. Between 800 – 1600 μs after t_o, high negative voltage are pulsed to both time-of-flight plates. The delay timing for electron filament supply and TOF plates need to be adjustable to suit different types of ion clusters. After extraction, the ions travelling through the time-of-flight tube will be separated according to mass. Before the laser interaction region, the mass gate and ion deceleration electrostatic lenses are pulsed to improve the mass selectivity and enhance the resolution. The pulsing of the mass gate and ion decelerator stack are referenced to the firing of the TOF plates pulse and the delay depends on the mass of ion to be isolated and then decelerated.

Simultaneously, on the master delay generator, a delay of 850 – 1650 μs based on t_o is set for the laser firing command (LFC). This delay is adjusted to match the flight of the ion of interest as it travels through the laser interaction chamber. The LFC is further divided into two pulses, flash lamp ignition and Q-switch flashing. The ignition of flash lamp is referenced to the LFC and 189 μs later, the Q-switch is flashed and the energy in the laser cavity is released. The electromagnet is also referenced to the LFC, however at a shorter delay of 183 μs. This arrangement allows the electromagnetic guiding field to be established in preparation for the photodetachment that will occur 6 μs later.

The bottom insets of Figure 23 illustrate mass and photoelectron spectra with respect to the timing scheme of the TOF-PES.

2.2 Theoretical aspects – *ab initio* methodology

Although fluoride acetylene clusters have been characterised in previous work by infrared spectroscopy[12] and *ab initio* calculations[36], they has not been treated with photoelectron spectroscopy, as such, *ab initio* computations are undertaken to predict the photoelectron spectra.

Optimisation of the cluster geometry is the first essential step for *ab initio* computation. In this thesis, the geometry of the fluoride acetylene cluster were optimised using Møller Plesset 2nd order perturbation theory[37] with Dunning's augmented correlation consistent polarised valence double and triple zeta (aug-cc-pVxZ , x = D and T) basis set under 'VeryTight' convergence criterion for the anion and neutral using GAUSSIAN98 and later GAUSSIAN03. All the calculations involving the neutral clusters are performed with Unrestricted Hartree Fock (UHF) wavefunction, so as to remove the degeneracy of electrons with antiparallel spin in the same orbital. Harmonic vibrational frequencies were also computed to determine the nature of the optimised geometry. Frequency calculations yielding imaginary frequencies correspond to structures which are either transition states or higher order maxima on the system's potential energy surface (section 1.2).

 The next procedure after acquiring the optimised structures is to construct potential energy surfaces. For the prediction of photoelectron spectra, the potential energy surfaces for both the anion and neutral complexes are required. A fluoride acetylene complex consists of five atoms and using the optimised geometry for an anion complex as the starting geometry, the latter's linear structure works out to have ten degrees of freedom of motion from 3N – 5, where N is the number of atoms in the molecule. This relates to ten different variables that will affect the potential energy

surface. In this theoretical investigation, the two modes of variables chosen for the computation of potential energy surface are varying (i) the distance between fluoride anion and acetylene and (ii) the angle between the fluoride and the intra molecular axis of the acetylene. The neutral complexes will be treated with the same geometrical manipulation as the anions; the two variables are given in Figure 24. A three-dimensional potential energy surfaces are constructed by varying the intermolecular distance (i) and angle (ii) on the *xy*-axes, while viewing the energy changes on the *z*-axis.

(i)

Figure 24. *Two variables for computing the potential energy surface*

(ii)
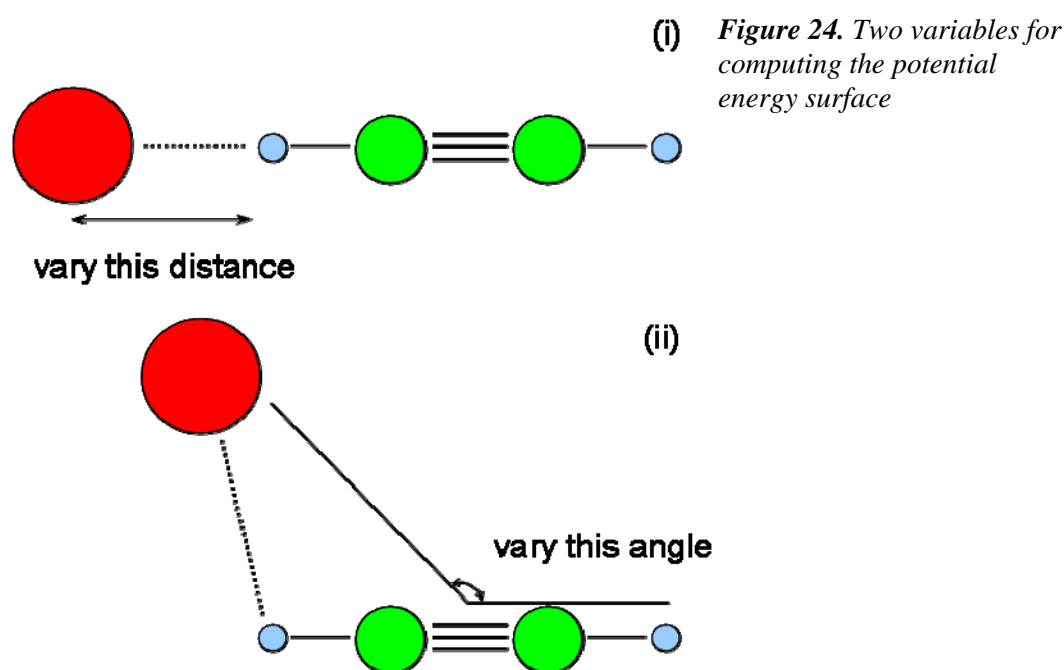
Prior to undertaking full modelling of the photoelectron spectra, a one dimensional potential energy curve can be used, i.e. intermolecular stretch. The fluoride acetylene complex is assumed to be a pseudo diatomic molecule, with fluoride anion on its own and acetylene collapsed on to its centre of mass. A software package, LEVEL 8.0[38] is used to calculate the vibrational wavefunctions of each 1-D curve by solving the radial Schrödinger equation. Franck-Condon overlap factors are then computed with reference to both the anion and neutral potential energy curves.

In addition to the preceding calculations, the bonding nature between the atoms of the cluster will be analysed by Natural Bond Orbital (NBO) analysis.[39, 40] This method describes the nature of cluster formation by calculating the population of electrons in particular orbital types. The aim of this analysis is to verify ionic hydrogen bond formation between the fluoride and acetylene during cluster formation through electron donation from fluoride's lone pairs to the antibonding orbitals of the C-H groups of acetylene. With the *ab initio* computation program GAUSSIAN 03, population analyses are carried out on acetylene in three different situations. The first analysis consists of the bare acetylene molecule, the second analysis looks at the fluoride acetylene complex at an optimised geometry and in the third situation, the fluoride is replaced by a single negative point charge with the geometry of acetylene preserved from the second analysis. The last analysis is important for assessing the contribution of polarisation in the electron delocalisation.

3. The TOF-PES

3.1 Experimental results – Mass spectra

Initial tests were carried out using carbon tetrachloride in argon gas with the intention of recording a mass spectrum of chloride ions. Chloride ions were expected to give rise to a signal about 14 µs after the ions are extracted with energy of around 2.5 keV. However, these initial attempts were not successful; a number of problems were encountered and the major setback was "ringing" in the signal due to impedance mismatch between the detector and oscilloscope shown in Figure 25.
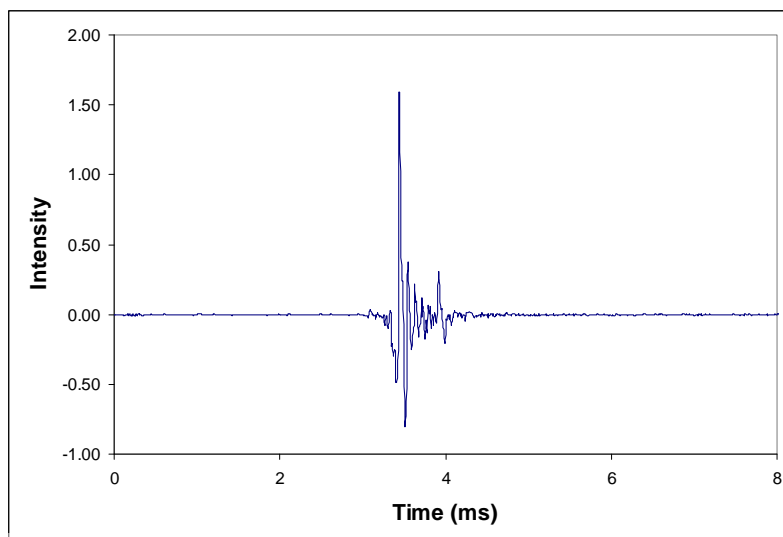
Figure 25. *Screenshot from the oscilloscope showing "ringing" in the signal*

After some corrections, the tests were resumed; unfortunately chloride ions are still not detected. Methyl iodide was chosen as the next halide precursor as the volatility of carbon tetrachloride was thought to be too low and the amount of vapour being delivered to the TOF-PES was insufficient.

A mass spectrum was obtained for methyl iodide and Figure 26 is a screenshot of the mass spectrum taken from the oscilloscope during one of the tests.
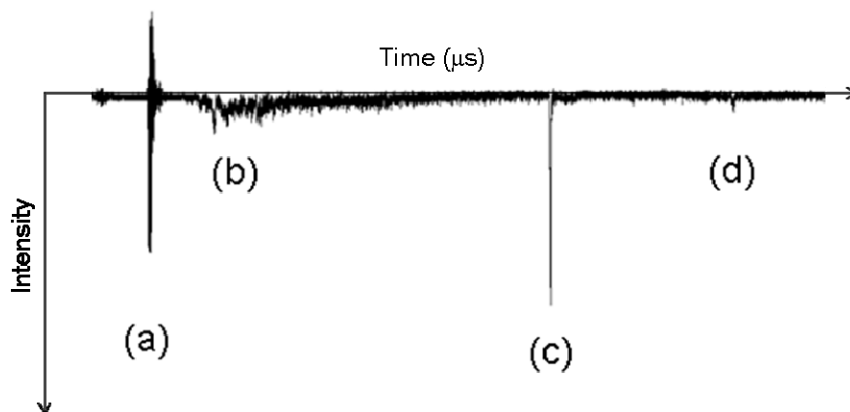
Figure 26. *Screenshot from the oscilloscope of the mass spectrum of the iodide anions.*

The sharp pulse shown at position (a) is noise from the extraction plate and that signifies the start of the ions' flight (*time* = 0 μs) down the time-of-flight axis. The band of signals that occur at position (b) were not assigned as they are detected about 3 μs after the extraction pulse and this short time-of-flight cannot be related to any known mass. The most likely assignment for these signals is to electrons which are present in the beam originating from the source chamber. The strong narrow peak at point (c) that was detected 24 μs after the extraction pulse is assigned to iodide anions and the small peak at position (d) could possibly be an $I^-\ldots[CH_3I]$ cluster as methyl iodide is used as a source of iodide anions in the supersonic expansion.

After the calibration of the gas mixing station pressure gauge, the apparatus is in a better position to be tested and optimised with more gaseous components in the gas expansion, such as acetylene. Figure 27 is a screenshot of a mass spectrum obtained for iodine acetylene clusters. Although the electron noise signal is still present in the early part of the spectrum, the quality of this spectrum is reasonable. The largest peak represents the bare iodide anion and the progression after this is assigned to clusters of I^--$[HCCH]_n$ with n = 1 to n=6 labelled respectively from peak (b) to (g). After peak (g), there is evidence of I^--[HCCH] clusters with up to nine acetylene ligands. The

intensities of these peaks are quite weak and are barely above the noise of the spectrum. Presence of other smaller peaks are also found along the base line and they are mostly likely due to I⁻…[Ar], I⁻…[H2O] and I⁻…[CH3I]. The actually assignment for these small peaks can only be made after calibration.
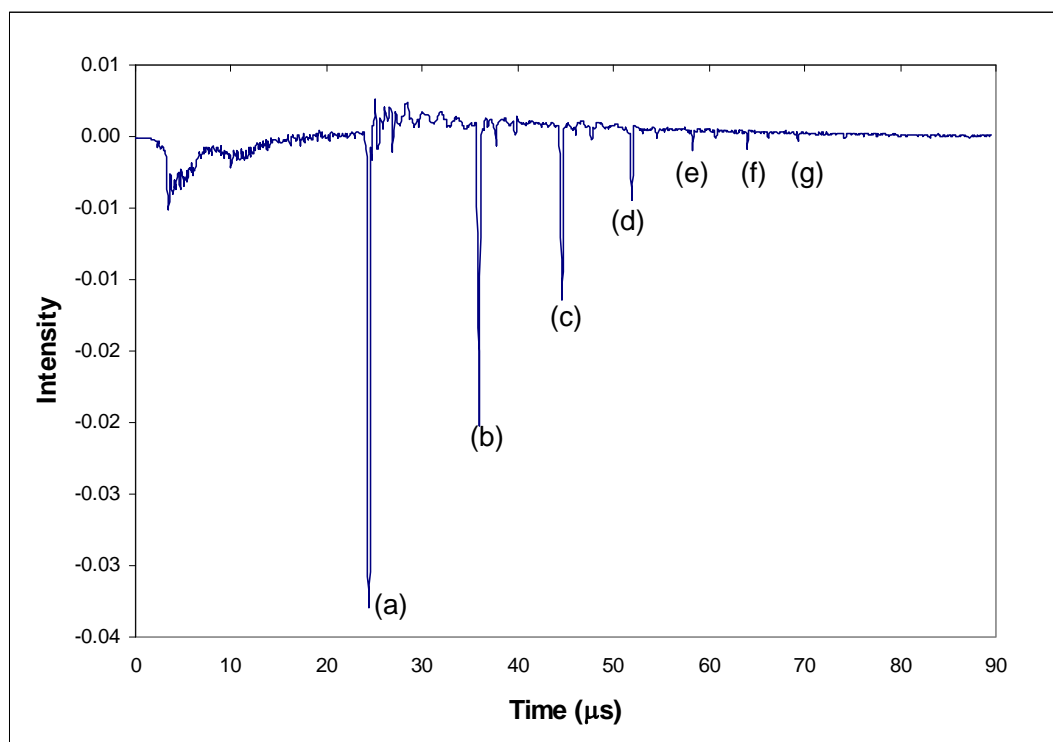
Figure 27. *Screenshot from the oscilloscope of I⁻, I⁻…[HCCH]ₙ with n = (1-6)*

Building upon the success with methyl iodide, dibromomethane was used as the next testing agent. With a natural abundance of approximately 50% for the ^{79}Br and ^{81}Br isotopes one would expect a doublet of approximately equal intensity in the mass spectrum. This feature would be prominent and provide a better "visual" aid for signal optimisation.
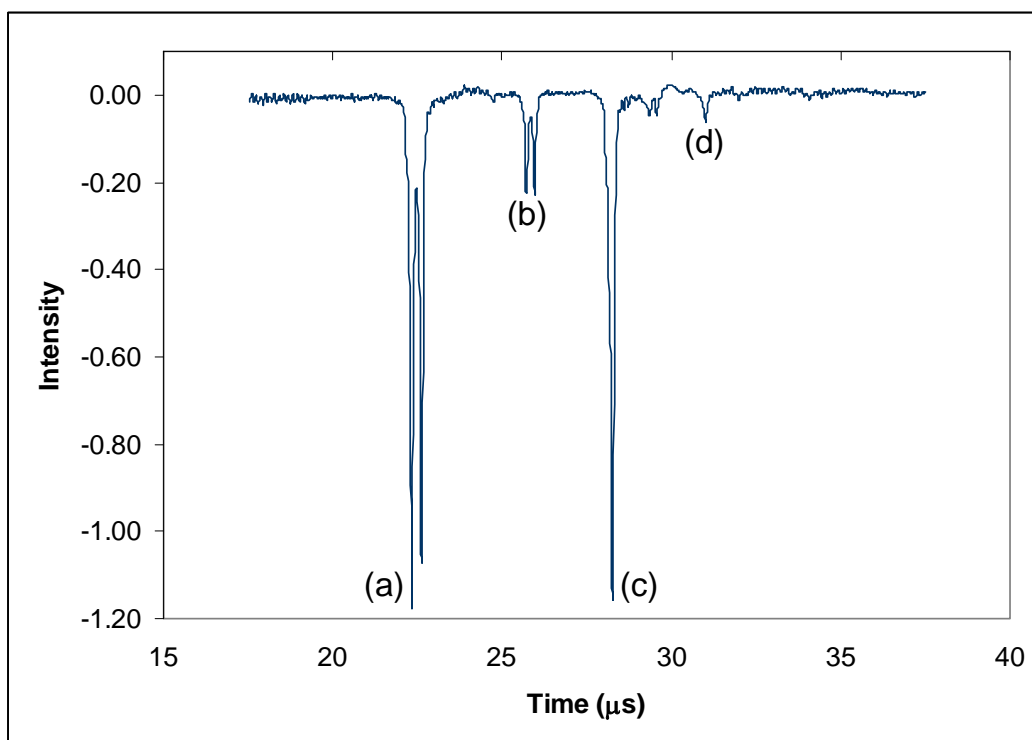
Figure 28a. Screenshot from the oscilloscope of Br⁻, Br⁻… [HCCH], I⁻ and I⁻…[HCCH]

The resulting time of flight spectrum of the bare bromide anion and bromide acetylene clusters is given in Figure 28a and a processed mass spectrum with the x-axis transformed to m/z is given in Figure 28b.

From the introduction section, it is assumed that the ions leave the extraction chamber with the same amount of potential energy and given

$$\text{P.E.} \quad = \quad q \cdot U \qquad (9)$$

where q is the charge of ion and U, the potential of the extraction field. Mass separation takes place according to equation 7 and hence the relationship between time-of-flight and mass/charge ratio can be derived from these two equations to give,

$$t \quad = \quad \frac{d}{\sqrt{2U}} \sqrt{\frac{m}{q}} \qquad (10)$$

where time-of-flight, t is related to $\sqrt{\dfrac{m}{q}}$ and $\dfrac{d}{\sqrt{2U}}$ are the known constants.

The doublet (a) corresponds to the ^{79}Br and ^{81}Br isotopes, the bromide ion with one acetylene molecule complex gives rise to a doublet (b), the singlet peaks at (c) and (d) are iodide ion and iodide with one acetylene complex. The iodide species are produced by the trace amounts of methyl iodide from previous experiments. Under careful examination, a weak doublet can be seen between peaks (c) and (d), that would most likely correspond to bromide with two acetylene molecules clusters
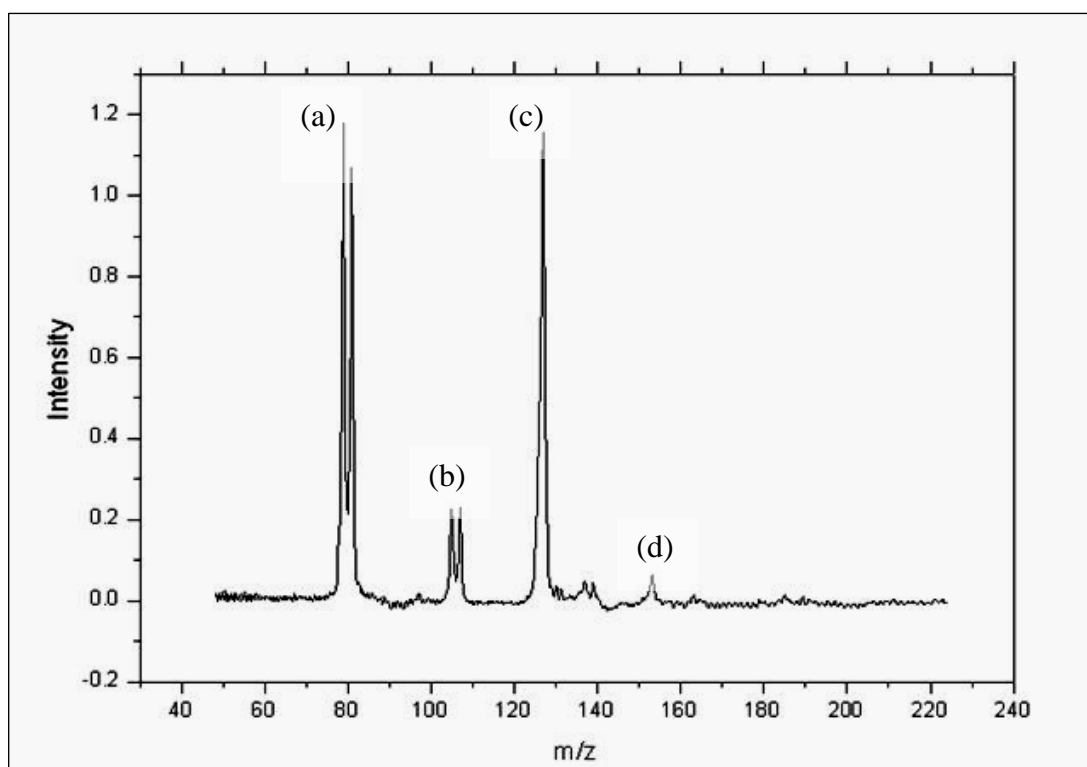
Figure 28b. *Mass spectrum showing Br⁻, Br⁻…[HCCH], I⁻ and I⁻…[HCCH]*

3.2 Experimental discussion

Among the upgrades, the modifications to the xy deflection plates and impedance matching of the detectors to the oscilloscope have had the biggest contribution towards the enhancement of signal detection. The ion beam position can now be adjusted with more sensitivity and alignment through the apparatus is achieved more easily. The signal to noise ratio is greatly enhanced; and clear evidence of ionic clusters is seen. The mass spectra shown in the result section is a good indication of these outcomes. Some of the new implementations might not have a huge influence on the final spectra but these optimisation efforts must be viewed as a whole entity. For example, the new monitoring routine of the safety system has proven to be very robust and as a result the frequency of pump trips has been reduced dramatically. This ensures that the high vacuum is maintained and experiments can be conducted conveniently at these optimum conditions.

The importance of high vacuum in the apparatus cannot be stressed enough. Apart from fulfilling its primary duty of minimising the presence of background gas, high vacuum also plays an important part in supersonic expansion of the gas mixture. Increasing the pumping efficiency in the source chamber, (i.e. where the expansion of gas occurs), definitely improves the thermodynamics of the gas expansion. Hence, a cryotrap is planned to be installed in the source chamber and construction is already under way.

It should be noted that the aforementioned success with the mass spectra were not produced readily before the acquisition of a new pulsed negative power supply for the electron supply filaments. The old power supply was incapable of supplying a stable voltage for thermionic emission and has been a major hindrance to the optimisation

progress. Presently, remodelling work is being carried out on the old power supply based on the circuitry design of the current one. Upon completion, it should also have the pulsed functionality with adjustable pulse delay and pulse width.

The optimisation process in still not complete and there are issues that still require much attention. From Figure 26 and 27, it is clear that one of the problems that still persist is the noise due to excessive background electrons. Apparently, the combined effort of wire mesh and graphite coating to enhance ground potential around the source assembly is insufficient to reduce stray electrons. The pulsed power supply did not reduce the amount of electrons produced by the filaments; however the massive electron noise is still being detected. While iodide and bromide ions can still be detected in the presence of the noise, the same cannot be said for the ions with a lighter mass. This could be the real reason for not being able to detect chloride ions as the electron noise spans from 3 µs to 15 µs and chloride ions were estimated to arrive between 13-14 µs. To address this, several ideas have been suggested[41] and that includes employing additional electric or magnetic field to divert the electrons while keep the magnitude of the field small so that the ions of interest will not be affected. Another method would be to gate the microchannel plate[42] so that the MCP will not get saturated by the electrons that arrive earlier then the ions of interest.

Apart from implementing new modifications and installing new components to the apparatus, some consideration should also be given to how the experiments are carried out. By varying the operating conditions, for example, having a greater backing pressure from the gas mixing station to the nozzle might change the expansion characteristics of the gas and clustering behaviour. At present, the gas is delivered

with a backing pressure of 100 psi and pulsed at 10 Hz repetition. A different backing pressure and repetition can be trialled in future as it had been proven that with a backing pressure of 40 psi at 20 Hz works well for $I_2^-\cdot[CO_2]$ clusters.[43]

Another operating parameter that might affect the mass resolution is the extraction energy applied to the TOF plates. As mentioned, a lower extraction energy will result a longer time-of-flight for the ions and various groups have employed different values of the extraction voltages that work best for specific ion clusters. Lower extraction energy may not improve the mass resolution due to temporal distributions but the longer time-of-flight would allow the electro-optics, i.e. ion decelerator, more time to influence the ions to achieve the latter effect. More importantly, adjustment to the TOF extraction field to achieve correct space focusing of the ions is still the most effective route to maximise detection.

4. *Ab initio* Calculation

4.1 Optimised geometries

The anion complex comprises a fluoride anion (charge of -1, multiplicity of 1) and a neutral acetylene molecule, while for the neutral counterpart, a fluorine atom (charge of 0, multiplicity of 2) replaces the anion. *Ab initio* calculations are also carried out on the acetylene subunit as a basis for comparison and these data are presented in Table 2. The calculated IR frequencies and intensities (given in bold, units of km/mol) are compared with experimental data[44] and the differences are given in parentheses. The symmetric C-C stretch is labelled ω_1, symmetric and anti-symmetric stretches of C-H are denoted by ω_2 and ω_3 respectively. The two doubly degenerate bending modes are labelled as ω_4 and ω_5. These data of bare acetylene molecule will be compared later to acetylene in the complexes. The theoretical values of the energies will be used to aid experiments when calculating the vertical detachment energy (VDE). The labelling of the atoms of the acetylene, i.e. from left to right, will be used throughout this thesis for the sake of consistency.

Figure 29. *Atoms of acetylene molecule with their respective labels*

Table 2. Optimised geometry and energy of the bare acetylene molecule with vibrational frequencies and IR intensity shown in bold at MP2/aug-cc-pVXZ (X=D,T) level of theory

	pVDZ		pVTZ	
Bonds	**Length (Å)**			
$r(H_a C_a)$	1.0753		1.0617	
$r(C_a C_b)$	1.2315		1.2122	
$r(C_b H_b)$	1.0753		1.0617	
	Wavenumber (cm^{-1})			
ω_1 σ_g	1946(28)	**0**	1968(6)	**0**
ω_2 σ_g	3519(145)	**0**	3534(160)	**0**
ω_3 σ_u	3431(142)	**93**	3432(143)	**96**
ω_4 π_g	409(203)	**0**	601(11)	**0**
ω_5 π_u	703(27)	**189**	754(24)	**180**
Energy	**E (Hartrees)**			
E_{MP2}	-77.092997		-77.164058	
ZPE	0.025335		0.026526	

The optimised geometry of anion complex is given in Figure 30 and the accompanying physical data calculated are presented in Table 3 and 4.
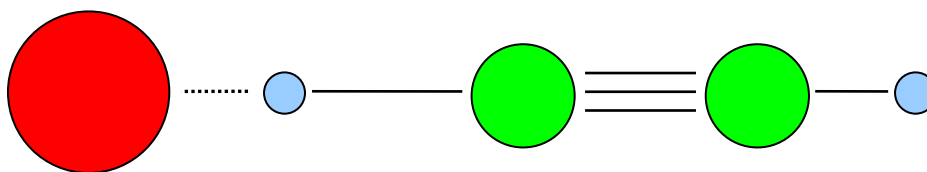
Figure 30. Optimised geometry of the anion F⁻...[HCCH] complex

The formation of anion complex brings about a significant change in the acetylene molecule. It is noted that H_a is drawn towards the fluoride anion as the length between H_a and C_a has increased. The geometry optimisation was undertaken at the same level of theory but with pVTZ basis set and these data are given in Table 4. Similar geometrical changes occur for the acetylene unit with H_a now even closer to the fluoride anion. For both basis sets the closeness is a strong indication of hydrogen bonding, this is validated from further analysis later in this these (NBO section).

Table 3. Optimised geometry and energy of F⁻ ...[HCCH] at MP2/aug-cc-pVDZ level of theory with vibrational frequencies and IR intensity shown in bold

Bond	Length (Å)	Vibrational Frequencies				Energies (Hartrees)	
r(F H_a)	1.320	ω_1	σ	328	**691**	E_{MP2}	-176.796820
r(H_a C_a)	1.238	ω_2	σ	1074	**3310**	ZPE	0.024013
r(C_a C_b)	1.250	ω_3	σ	2043	**306**		
r(C_b H_b)	1.076	ω_4	σ	3452	**3**		
		ω_5	π	172	**<1**		
		ω_6	π	448	**113**		
		ω_7	π	1202	**93**		

Table 4. Optimised geometry and energy of F⁻ ...[HCCH] at MP2/aug-cc-pVTZ level of theory with vibrational frequencies and IR intensity shown in bold

Bond	Length (Å)	Vibrational Frequencies				Energies (Hartrees)	
r(F H_a)	1.125	ω_1	σ	303	**1203**	E_{MP2}	-176.947093
r(H_a C_a)	1.395	ω_2	σ	830	**3562**	ZPE	0.024045
r(C_a C_b)	1.239	ω_3	σ	1933	**15**		
r(C_b H_b)	1.065	ω_4	σ	3440	**2**		
		ω_5	π	166	**13**		
		ω_6	π	577	**125**		
		ω_7	π	1281	**85**		

For the neutral complex, two optimised geometries were found. The first configuration, referred to as "neutral T-shape" is shown in Figure 31 with the computed physical data presented in Table 5 and 6. This fluorine atom resides near the centre of the acetylene molecule over the triple bond and hence maximising the
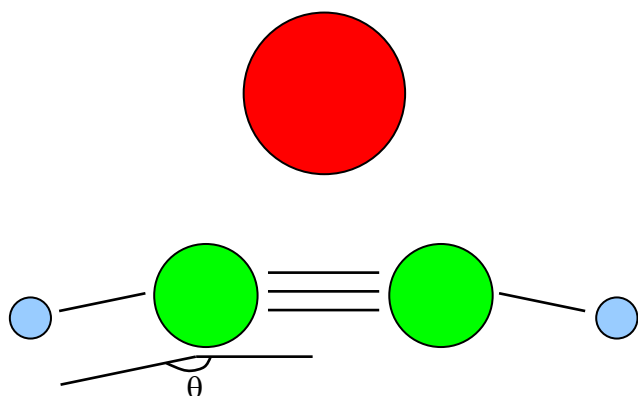
dispersion interaction between the two species. Both C-H bonds are forced away from the fluorine atom and the linearity of acetylene is broken, reducing the overall symmetry of the complex to C_{2v}.

Figure 31. First optimised geometry of the neutral F…[HCCH] complex

Table 5. Optimised geometry and energy of neutral T- shape F…[HCCH] complex at uMP2/aug-cc-pVDZ level of theory with vibrational frequencies and IR intensity shown in bold

Bond	Length (Å)	Angle	(degrees)	Vibrational Frequencies		Energies (Hartrees)	
$r(H_a C_a)$	1.076	$\theta(H_a C_a C_b)$	176.9	A1	386	**32**	E_{MP2}	-176.635461
$r(C_a F)$	1.981	$\theta(F\ C_a C_b)$	71.6	A1	730	**81**	ZPE	0.052738
$r(F C_b)$	1.981	$\theta(C_a C_b H_b)$	176.9	A1	1851	**92**		
$r(C_a C_b)$	1.251			A1	3506	**6**		
$r(C_b H_b)$	1.076			A2	384	**0**		
				B1	675	**86**		
				B2	524	**2**		
				B2	3398	**407**		
				B2	11695	**515160**		

Table 6. Optimised geometry and energy of neutral T-shape F…[HCCH] complex at uMP2/aug-cc-pVTZ level of theory with vibrational frequencies and IR intensity shown in bold

Bond	Length (Å)	Angle	(degrees)	Vibrational Frequencies		Energies (Hartrees)	
$r(H_a C_a)$	1.063	$\theta(H_a C_a C_b)$	177.0	A1	386	**32**	E_{MP2}	-176.782630
$r(C_a F)$	1.963	$\theta(F\ C_a C_b)$	71.7	A1	770	**76**	ZPE	0.034141
$r(F C_b)$	1.963	$\theta(C_a C_b H_b)$	177.0	A1	1869	**90**		
$r(C_a C_b)$	1.233			A1	3517	**7**		
$r(C_b H_b)$	1.063			A2	593	**0**		
				B1	730	**82**		
				B2	587	**3**		
				B2	3031	**2278**		
				B2	3505	**141**		

The second optimised geometry of the neutral complex, referred to as "neutral linear"

is shown in Figure 32 and the associated physical data in Table 7 and 8.
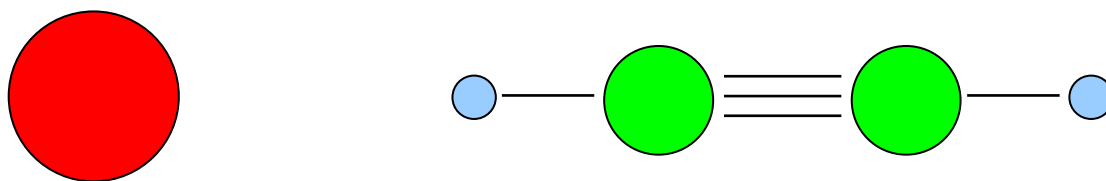
Figure 32. *Second optimised geometry of the neutral F…[HCCH] complex*

Compared to the analogous anion-acetylene geometry the interaction between fluorine

and acetylene is weaker as the species are further apart. The geometry of acetylene

subunit is barely changed from that of the bare molecule.

Table 7. Optimised geometry and energy of linear neutral F…[HCCH] complex at uMP2/aug-cc-pVDZ level of theory with vibrational frequencies and IR intensity shown in bold

Bond Length (Å)		Vibrational Frequencies				Energies (Hartrees)	
$r(F\,H_a)$	2.444	ω_1	σ	71	**<1**	E_{MP2}	-176.629916
$r(H_a\,C_a)$	1.076	ω_2	σ	1950	**<1**	ZPE	0.025912
$r(C_a\,C_b)$	1.232	ω_3	σ	3432	**124**		
$r(C_b\,H_b)$	1.075	ω_4	σ	3519	**2**		
		ω_5	π	54	**<1**		
		ω_6	π	61	**<1**		
		ω_7	π	426	**<1**		
		ω_8	π	428	**<1**		
		ω_9	π	715	**94**		
		ω_{10}	π	718	**91**		

Table 8. Optimised geometry and energy of linear neutral F…[HCCH] complex at uMP2/aug-cc-pVTZ level of theory with vibrational frequencies and IR intensity shown in bold

Bond Length (Å)		Vibrational Frequencies				Energies (Hartrees)	
$r(F\,H_a)$	2.467	ω_1	σ	68	**<1**	E_{MP2}	-176.777234
$r(H_a\,C_a)$	1.062	ω_2	σ	1967	**<1**	ZPE	0.027033
$r(C_a\,C_b)$	1.212	ω_3	σ	3432	**124**		
$r(C_b\,H_b)$	1.062	ω_4	σ	3534	**3**		
		ω_5	π	51	**<1**		
		ω_6	π	56	**<1**		
		ω_7	π	613	**<1**		
		ω_8	π	614	**<1**		
		ω_9	π	764	**89**		
		ω_{10}	π	767	**86**		

The most significant observation change of the acetylene is the increase in HaCa bond length upon the formation of F⁻…[HCCH] anion complex. According to the calculation with pVTZ basis, the geometry reveals that Ha is bound closer to the fluorine then the alkynic carbon. The equilibrium bond lengths of F⁻…[HCCH] anion complex from previous calculations [36] have displayed this similar trend and their results are compiled in Table 9 for comparison.

Table 9. Comparison of equilibrium bond lengths (in Å) for F⁻…[HCCH] complex calculated from different level of theories

Method	$r(F\,H_a)$	$r(H_a\,C_a)$	$r(C_a\,C_b)$	$r(C_b\,H_b)$
MP2 [a]	1.1250	1.3950	1.2390	1.0650
SCF [b]	0.9709	1.6827	1.2129	1.0557
MP2 [b]	1.1071	1.4183	1.2363	1.0645
CCSD(T) [b]	1.0542	1.5029	1.2365	1.0672

[a] Calculated bond lengths reported in this thesis based on aug-cc-pVTZ
[b] Calculated bond lengths from reference[36] based on aug-cc-pVQZ

While a fairly good comparison can be drawn between the results for the equilibrium bond lengths, the same cannot be said for the harmonic stretching vibrational wavenumbers. The reported figures and the corresponding mode of vibrations are presented in Table 10. Apart from the stretch at the proton bridge, the rest of the frequencies were similar. This discrepancy is probably due to the level of theory used during calculation. At CCSD(T) level of theory, the correlation between electrons are calculated with more determinants, therefore, the FH stretch which is heavily involved with electron transfer are simulated with a better

Table 10. Comparison of stretching vibrational frequency for F⁻…[HCCH] complex

Stretching mode		CCSD(T) [b]	MP2 [a]
		ω (cm^{-1})	
Outer CH Stretch	($C_b H_b$)	3397	3440
CC stretch	($C_a C_b$)	1942	1932
FH stretch		1584	829
Intermolecular stretch		305	303

[a] Vibrations reported in this thesis based on aug-cc-pVTZ
[b] Vibrations from reference[36] based on aug-cc-pVQZ

accuracy. In order to draw a better comparison, the present frequency calculation should be performed at a higher level of theory, i.e. MP4.

The F…[HCCH] neutral complex has not been probed by *ab initio* calculation previously; therefore, it is only reasonable to compare the obtained result from the two basis sets used against well known experimental data of the bare acetylene molecule.

Apart from the slight variation in vibrational frequencies, there is no obvious change between the acetylene subunit in the "neutral linear" cluster and the bare acetylene molecule. Most probably, the equilibrium intermolecular distance between the fluorine atom and acetylene molecule is too far apart for a strong interaction to occur. For the "neutral T-shape" counterpart, an exceptionally large vibrational frequency is noted for the "rocking" mode of the acetylene molecule. Since this phenomenon is not observed in the results calculated with pVTZ, it is most likely to be caused by a basis set effect and should this be checked by taking the vibrational analysis calculation to the next higher level basis set. It is also noted that "neutral T-shape" is the preferred geometry for the neutral complex as it has lower equilibrium energy.

Table 11. Predicted energetic values for fluoride-acetylene system at MP2 level of theory

Spectral constant F…HCCH system	pVDZ	pVTZ
	kJ.mol^{-1}	
VDE	484	439
Ea	443	454
Ea (F)	342	351

The energetic values for the fluoride-acetylene system are derived from the computed results and are provided in Table 11. Although these calculated values are to be verified by experimental photoelectron spectroscopy, some of them exceed the maximum amount of energy a 266 nm laser could afford. Hence, it will be prudent to verify these values again with calculation at a higher level of theory before proceeding with the experiments.

4.2 Natural bond orbital analyses

Natural Bond Orbital analyses have been performed to quantify the stabilisation of cluster formation and to rationalise the dominant intermolecular interactions. The data presented comprise orbital occupancies in milli-electrons $m\mathbf{e}$ and stabilisation energies afforded by electron delocalisation (in kcal.mol^{-1}).

A summary of the stabilisation energies associated with the electron delocalisation to the $C_a - H_a$ group of the acetylene unit is given in Table 12. The analyses were performed with both pVDZ and pVTZ basis sets, however conclusions drawn from these analysis are based on the results from the pVTZ level.

Table 12. Principal electron delocalisations indicative of H-bonding. Stabilisation energies are provided in kcal.mol^{-1}

Type of complex	Donor	Acceptor	Stabilisation energy	
			pVDZ Kcal/mol	**pVTZ** Kcal/mol
Anion cluster	CR (1) F	$\sigma^* C_a - H_a$	4.07	9.04
	LP (3) F	$\sigma^* C_a - H_a$	10.24	20.27
	LP (4) F	$\sigma^* C_a - H_a$	114.23	238.06
Neutral cluster - 'linear'	LP (2) F α	$\sigma^* C_a - H_a$	0.04	
	LP (4) F α	$\sigma^* C_a - H_a$	0.90	0.42
	LP (1) F β	$\sigma^* C_a - H_a$	0.03	
	LP (3) F β	$\sigma^* C_a - H_a$	0.96	0.50
Neutral cluster - 'T-shaped'	LP (4) F α	$\sigma^* C_a - H_a$	0.27	0.39
		$\sigma^* C_b - H_b$	0.27	0.39
	LP (3) F β	$\sigma^* C_a - H_a$	0.29	0.40
		$\sigma^* C_b - H_b$	0.29	0.40

A clear indication of hydrogen bonding is observed with the anion cluster as there is electron transfer from the lone pairs of the fluorine to the anti-bonding orbital of $C_a - H_a$ group of acetylene. The reduction in bonding character weakens the $C_a - H_a$ bond and caused the increase in bond length. The impact of this weakening is reflected in

the shift of the vibrational frequency to lower wavenumber. For both geometries of the neutral cluster a very small magnitude of the electron delocalisation observed as the stabilisation energy is very weak.

The effect of polarisation can be observed from the occupancy of the C-H groups of acetylene. From Table 13, the bare molecule displayed equal population of the σ^* anti-bonding orbital of both C-H groups (5.4 $m\mathbf{e}$). The effect of polarisation is observed when a point negative charge replaces the fluoride anion. In this example, the population of the C_b–H_b antibonding orbital is larger than that of the H_a–C_a indicating a shift in electron density away from the negative charge. In the anion complex, a significant increase in occupancy was observed due to the electron delocalisation from the fluoride anion and a higher occupancy is observed in σ^* orbital of H_a–C_a as this CH group is closer to the anion. In the neutral cluster, the change in occupancy of the H_a–C_a anti-bonding orbital is a slight indication of hydrogen bond formation. This is not observed in the 'T-shaped' geometry as the fluorine is saddled between the acetylene.

Table 13. Quantitative analysis on occupancy of H-C groups to indicate polarisation

| | Occupancy ($m\mathbf{e}$) | |
	$H_a – C_a$	$C_b – H_b$
Bare Acetylene	5.4	5.4
Acetylene with negative charge	2.2	9.9
Anion complex	21.2	11.9
Neutral complex - 'linear'		
- a spin orbital	3.3	2.7
- b spin orbital	3.5	2.7
Neutral complex - 'T-shaped'		
- a spin orbital	3.0	3.0
- b spin orbital	3.1	3.1

4.3 Two-dimensional potential energy surface

The anion complex is treated with the geometrical manipulation described in the material and methods section to obtain the two-dimensional potential energy surface. The scan is obtained at MP2/pVDZ level of theory to qualitatively assess the effect that intermolecular distance or angular interaction might have on the potential energy. Figure 33 shows that as the angle between the fluorine and the intramolecular axis of acetylene approaches 90°, the complex starts to lose its stability and become repulsive. This is observed as the fluoride anion gradually moves away from the C-H group of the acetylene and the stability from the hydrogen bonding is lost.
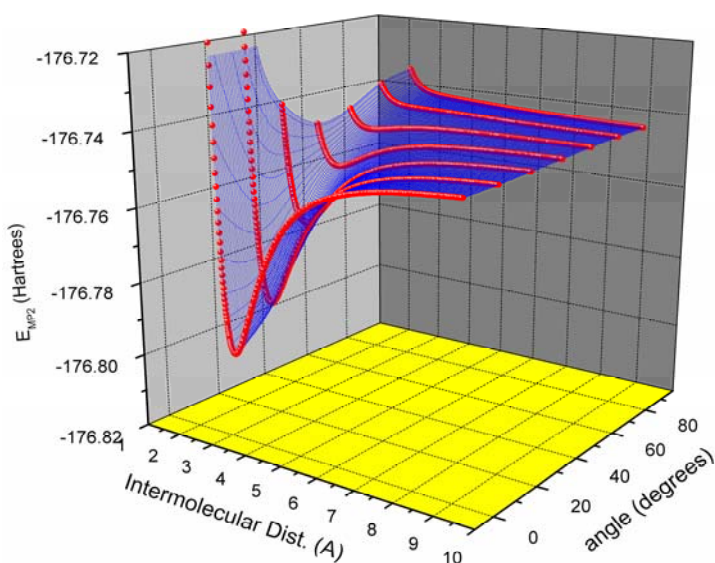
Figure 33. *Potential energy surface for $F^{-}...[HCCH]$ anion complex*

The neutral complex is treated in a slightly differently manner to the anion counterpart. As there are two known equilibrium geometries for the neutral cluster, Figure 34 shows how the energy changes between the two geometries with the projection on the YZ plane illustrating the change in depth on the potential energy surface. Using the optimised geometry of "neutral linear" as the starting point, the fluorine atom is being rotated 180° around the acetylene and with every 15° increment; the fluorine is brought in closer by 1.0 Angstrom. The result from the

scan agrees that the "neutral T-shaped" is the favoured geometry as it has a lower potential energy.
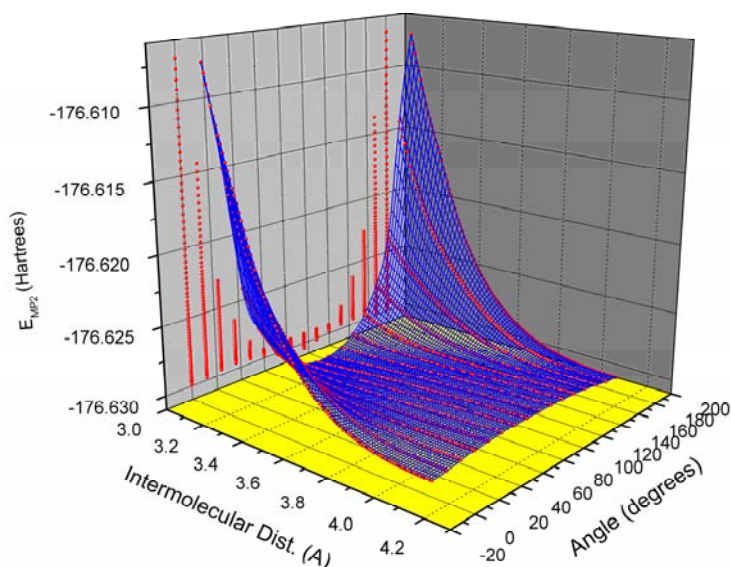
Figure 34. *Potential energy surface for F…[HCCH] neutral linear complex*

To reinforce that "neutral T-shape" is the preferred geometry, a relaxed potential energy scan was computated and shown in Figure 35. The fluorine was position perpendicular to a linear acetylene molecule, 4.1 angstrom away. The scan begins by bringing the fluorine atom closer while maintaining the 90° orientation with the acetylene. Interestingly, both C-H groups on the acetylene molecule start to flex as the
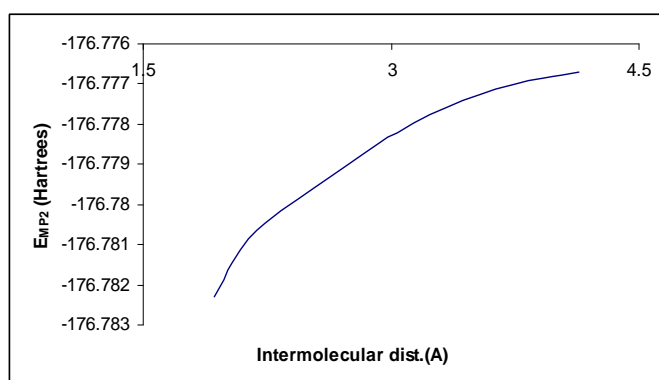
Figure 35. *Relaxed potential energy scan of neutral F…[HCCH]*

fluorine approaches and begin to resemble the optimised geometry of the "neutral T-shape" isomer. It should be noted that the energy final position is very close to the minimum energy obtain for "neutral T-shaped" at uMP2/pVTZ level of theory.

4.4 Predicted photoelectron spectra

One-dimension potential energy curves are obtained for the intermolecular stretch for both the neutral 'linear' and anion complex and these two curves are presented in Figure 36. The bottom curve which is derived from the anion complex has a 'deep well' characteristic of a tightly bound ion-molecule complex. This is supported by the NBO result which indicates a large extent of hydrogen bonding. The top curve belongs to the neutral 'linear' complex and the shallow potential is clear evidence of having low dissociation energy with a far weaker hydrogen bond.
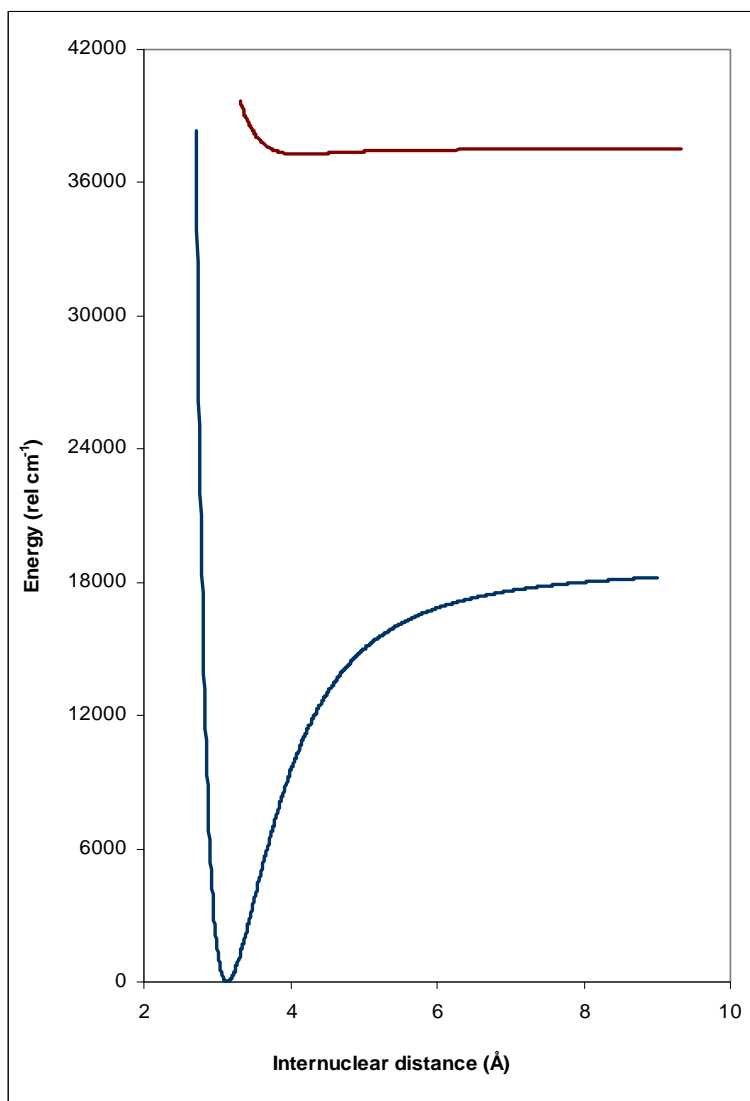
Figure 36. *One-dimensional potential energy curve for F⁻...[HCCH] anion complex (lower curve) and F...[HCCH] neutral complex (upper curve) at MP2/pVTZ level of theory*

The one dimensional radial Schrödinger equation was solved to produce intermolecular stretch vibrational wavefunctions and energy levels for the anion and neutral clusters so that the Franck-Condon factors can be calculated to predict the photoelectron spectrum. In order to appreciate how the vibrational wavefunction of

60

the anion surface overlaps with the most probable transition in the neutral surface, the

solutions to the neutral and anion vibrational wave function are presented in Figure

37.
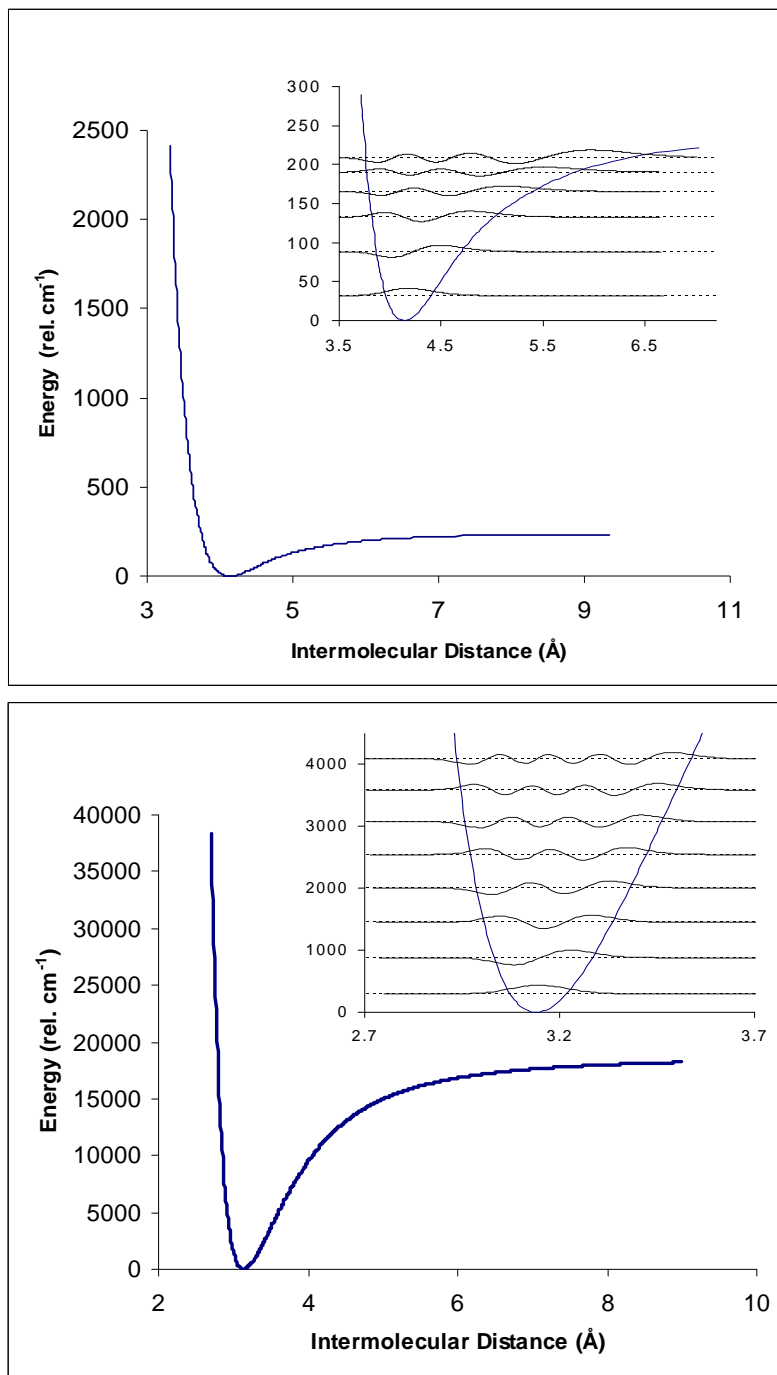
Figure 37. 1-D potential energy curve for F…[HCCH] neutral linear complex (top graph) and F⁻…[HCCH] anion complex (bottom graph) at MP2/aug-cc-pVTZ level of theory, with respective vibrational wavefunctions inset

The predicted photoelectron spectra for the F·[HCCH] system at MP2/aug-cc-pVDZ and pVTZ levels of theory are presented in Figure 38 and 39.
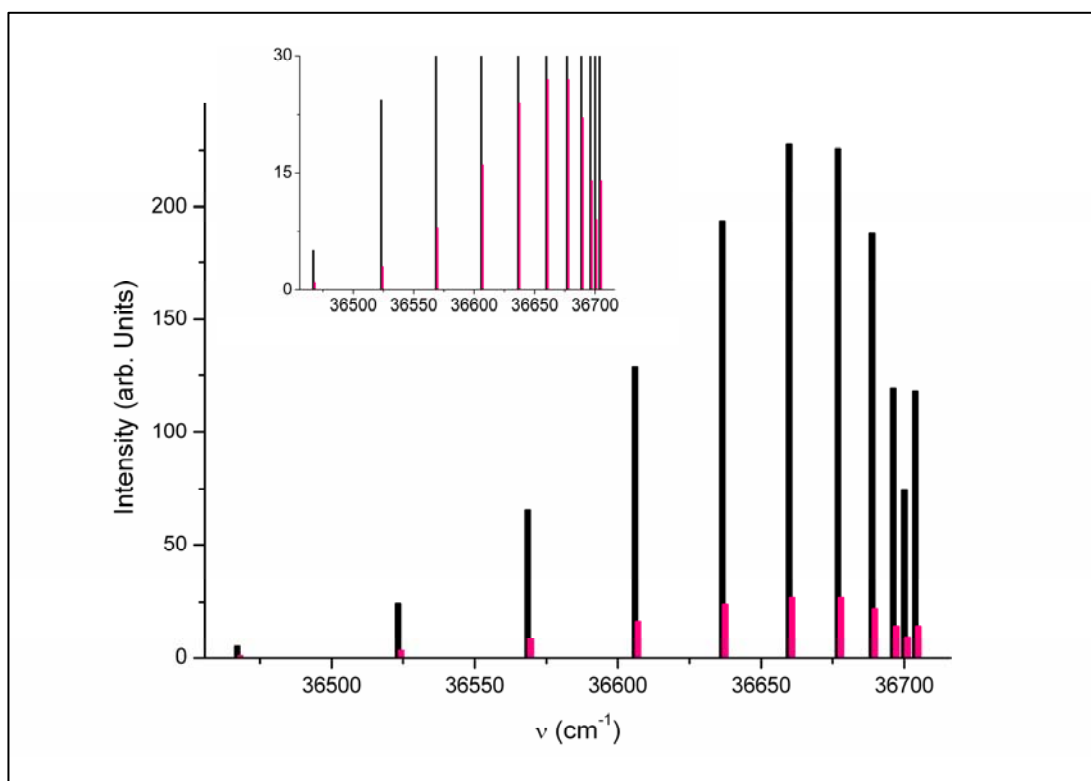
Figure 38. Predicted photoelectron spectra for F ·[HCCH] system using pVDZ basis set
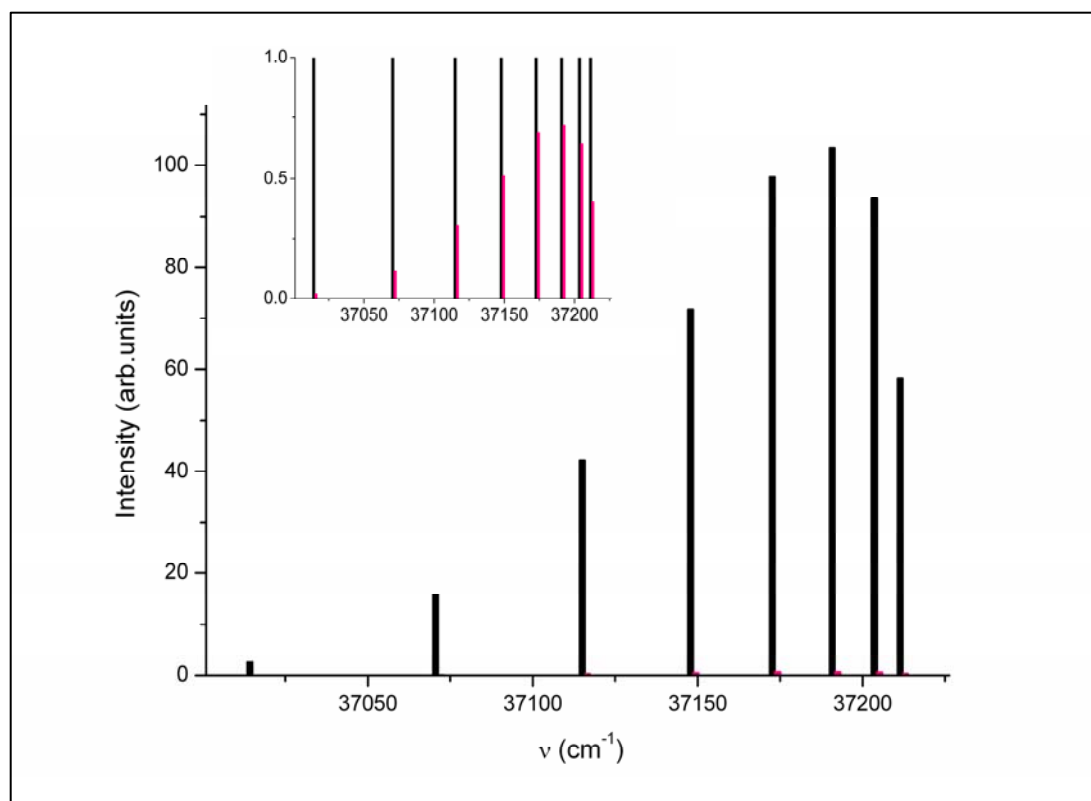
Figure 39. Predicted photoelectron spectra for F ·[HCCH] system using pVTZ basis set

At the MP2 level of theory, both pVDZ and pVTZ basis set shows a good degree of spectral agreement and suggest 5←0 transition as the most probable. The series of transitions originating from the anion v=1 vibrational level were also modelled and shown in pink in the figures. The magnitudes of the Franck-Condon factors were adjusted according to the vibrational partition function at a temperature of 50 K, which is a typical temperature of a cluster formed in a supersonic expansion. The intensities were much smaller and are shown as insets on the diagrams. It should be noted that while the spectra appear to be similar, the intensity of hot bands predicted at higher level basis set is apparently very much lower.

5. Conclusion and Future work

The experimental work detailed in this thesis describes most of the key modifications carried out on the time-of-flight mass spectrometer in tandem with the anion photoelectron spectrometer. The TOF-PES is now into the final phase of the optimisation progress and future work will include working towards better vacuum conditions, minimisation of the excessive noise from background electrons, finalising the pulse power supply for the electron filament and finally, the alignment of the optics for photodetachment.

The elementary theoretical calculations presented in this work outline the fundamental nature of fluorine – acetylene complexes and they are by no means a full representation of the cluster. Basic energetic values and physical properties are predicted, however, they are insufficient to serve as a guidance or prediction for the actual experiments as there are some discrepancies and uncertainty with the computation results. Future computation should be carried out at higher level of theory and larger basis set with the appropriate basis set correction so as to obtain a better prediction of the system.

6. References

1   D. A. Doyle, J. M. Cabral, R. A. Pfuetzner, A. Kuo, J. M. Gulbis, S. L. Cohen, B. T. Chait and R. MacKinnon, *Science*, 1998, **280**, 69.

2   M. V. Rodnina, M. Beringer and W. Wintermeyer, *Trends. Biochem. Sci.*, 2007, **32**, 20.

3   A.W. Castleman and R.G. Keesee, *Chem. Rev.*, 1986, **86**, 589.

4   P. Kebarle, *Ann. Rev. Phys. Chem.*, 1977, **28**, 445.

5   R.T. McIver Jr, *Rev. Sci. Instrum.*, 1970, **41**, 555.

6   E. J. Bieske and O. Dopfer, *Chem. Rev.*, 2000, **100**, 3963.

7   U. Boesl, C. Bämann and R. Käsmeier, *Int. J. Mass. Spectrom.*, 2001, **206**, 231.

8   O. Cheshnovsky, S.H. Yang, C.L. Pettiette, M.J. Craycraft and R.E. Smalley, *Rev. Sci. Instrum.*, 1987, **58**, 2131.

9   J. Simons, *J. Chem. Phys.*, 2008, **112**, 6401.

10   D.A. Wild and E. J. Bieske, *Int. Rev. Phys. Chem.*, 2003, **22**, 129.

11   E. J. Bieske, *Chem. Soc. Rev.*, 2003, **32**, 231.

12   D.A. Wild, Z.M. Loh, R.L. Wilson and E.J. Biesks, Unpublished work for F^- $(HCCH)_n$, n = 3-6.

13   G. Czako, B.J. Braams and J. M. Bowman, *J. Phys. Chem. A*, 2008, **112**, 7466.

14   M.S. Johnson, K.T. Kuwata, C. Wong and M. Okumura, *Chem. Phy. Lett.*, 1996, **260**, 551.

15   U. Boesl and W.J. Knott, *Mass. Spectrom. Rev.*, 1998, **17**, 275.

16   O. Dopfer and v. Engel, *J. Chem. Phys.*, 2004, **121**, 12345.

17   K.R. Asmis, T.R. Taylor and D.M. Neumark, *Chem. Phy. Lett.*, 1998, **295**, 75.

18   N.L. Pivonka, C. Kaposta, M. Brummer, G. von Helden, G. Meijer, L. Woste, D.M. Neumark and K.R. Asmis, *J. Chem. Phys.*, 2003, **118**, 5275.

19   M.Okumura, L.I. Yeh, J.D. Myers and Y. T. Lee, *J. Chem. Phys.*, 1986, **85**, 2328.

20   J. M. Hollas, *Modern Spectroscopy, 4th edition*, John Wiley & Sons, Chichester,UK, 2004.

21   J. H. D. Eland, *Photoelectron Spectroscopy, 2nd edition*, Butterworth, Southampton,UK, 1984.

22   W. C. Wiley and I.H. McLaren, *Rev. Sci. Instrum.*, 1955, **26**, 1150.

23   J. L. Wiza, *Nucl. Instrum. Meth.*, 1979, **162**, 587.

24   K. Muller-Dethlefs and E.W. Schlag, *Ann. Rev. Phys. Chem.*, 1991, **42**, 109.

25   Y.X. Zhao, C.C. Arnold and D.M. Neumark, *Faraday Trans*, 1993, **89**, 1449.

26   A.Osterwalder, M.J. Nee, J. Zhou and D.M. Neumark, *J. Chem. Phys.*, 2004, **121**, 6317.

27   *Gaussian 03, Revision E.01, M. J. Frisch, G. W. Trucks, H. B. Schlegel, G. E. Scuseria, M. A. Robb, J. R. Cheeseman, J. A. Montgomery, Jr., T. Vreven, K. N. Kudin, J. C. Burant, J. M. Millam, S. S. Iyengar, J. Tomasi, V. Barone, B. Mennucci, M. Cossi, G. Scalmani, N. Rega, G. A. Petersson, H. Nakatsuji, M. Hada, M. Ehara, K. Toyota, R. Fukuda, J. Hasegawa, M. Ishida, T. Nakajima, Y. Honda, O. Kitao, H. Nakai, M. Klene, X. Li, J. E. Knox, H. P. Hratchian, J. B. Cross, V. Bakken, C. Adamo, J. Jaramillo, R. Gomperts, R. E. Stratmann, O. Yazyev, A. J. Austin, R. Cammi, C. Pomelli, J. W. Ochterski, P. Y. Ayala, K. Morokuma, G. A. Voth, P. Salvador, J. J. Dannenberg, V. G. Zakrzewski, S. Dapprich, A. D. Daniels, M. C. Strain, O. Farkas, D. K. Malick, A. D. Rabuck, K. Raghavachari, J. B. Foresman, J. V. Ortiz, Q. Cui, A. G. Baboul, S.*

Clifford, J. Cioslowski, B. B. Stefanov, G. Liu, A. Liashenko, P. Piskorz, I. Komaromi, R. L. Martin, D. J. Fox, T. Keith, M. A. Al-Laham, C. Y. Peng, A. Nanayakkara, M. Challacombe, P. M. W. Gill, B. Johnson, W. Chen, M. W. Wong, C. Gonzalez, and J. A. Pople, Gaussian, Inc., Wallingford CT, 2004.

28   M.W. Schmidt, K.K. Baldridge, J.A. Boatz, S.T. Elbert, M.S. Gordon, J.J. Jensen, S. Koseki, N. Matsunaga, K.A. Nguyen, S. Su, T.L. Windus, M. Dupuis and J. A. Montgomery, GAMESS Version 21, 1995.

29   *Courtesy of Dr. Allan McKinley.*

30   *Courtesy of A/Prof Evan Bieske, UniMelb.*

31   P. Schwartze, H. Baumgartel and C. Eisenhardt, *Rev. Sci. Instrum.*, 2001, **72**, 3125.

32   *BASIC programming code by Dr. Duncan Wild.*

33   J. Cooper and R.N. Zare, *J. Chem. Phys.*, 1967, **48**, 942.

34   S.E. Bradforth, D. W. Arnold, D.M. Neumark and D.E. Manolopoulos, *J. Chem. Phys.*, 1933, **99**, 6345.

35   J.B. Cui, M. Stammler, J. Risein and L. Ley, *J. Appl. Phys.*, 2000, **88**, 3667.

36   P. Botschwina, T. Dutoi, M. Mladenovic, R. Oswald, S. Schmatz and H. Stoll, *Faraday. Discuss.*, 2001, **118**, 433.

37   C. Møller and M.S. Plesset, *Phys. Rev.*, 1934, **46**, 618.

38   R.J. Le Roy, LEVEL 8.0: *A Computer Program for Solving the Radial Schrodinger Equation for Bound and Quasibound Levels*, University of Waterloo Chemical Physics Research Report CP-663 (2007); see http://leroy.uwaterloo.ca/programs/ .

39   J. P. Foster and F. Weinhold, *J. Am. Chem. Soc.*, 1980, **102**, 7211.

40   *NBO 5.0. E. D. Glendening, J, K. Badenhoop, A. E. Reed, J. E. Carpenter, J. A. Bohmann, C. M. Morales, and F. Weinhold, Theoretical Chemistry Institute, University of Wisconsin, Madison (2001).*

41   *Based on results from simulations carried out by Dr. D. Wild.*

42   M. Gostein and G.O. Sitz, *Rev. Sci. Instrum.*, 1995, **65**, 3389.

43   H. Gomez, T. R. Taylor and D.M. Neumark, *J. Chem. Phys.*, 2002, **116**, 6111.

44   T. Shimanouchi, *Tables of Molecular Vibrational Frequencies Consolidated Volume I*, National Bureau of Standards, **1972**, 1-160.